NASA TECHNICAL NOTE

NASA TN D-5816

c. 1

NASA TN D-5816

TECH LIBRARY KAFB, NM
0132538

LOAN COPY: RETURN TO
AFWL (WLOL)
KIRTLAND AFB, N MEX

STATIC AERODYNAMIC CHARACTERISTICS, PRESSURE DISTRIBUTIONS, AND RAM-AIR INFLATION OF ATTACHED INFLATABLE DECELERATOR MODELS AT MACH 3.0

RECEIVED
MAY 1970
Technical Library
AFWeapons
Laboratory

by William D. Deveikis and James Wayne Sawyer

Langley Research Center
Hampton, Va. 23365

NATIONAL AERONAUTICS AND SPACE ADMINISTRATION • WASHINGTON, D. C. • MAY 1970

TECH LIBRARY KAFB, NM

0132538

1. Report No. NASA TN D-5816	2. Government Accession No.	3. Recipient'
4. Title and Subtitle STATIC AERODYNAMIC CHARACTERISTICS, PRESSURE DISTRIBUTIONS, AND RAM-AIR INFLATION OF ATTACHED INFLATABLE DECELERATOR MODELS AT MACH 3.0		5. Report Date May 1970
		6. Performing Organization Code
7. Author(s) William D. Deveikis and James Wayne Sawyer		8. Performing Organization Report No. L-6337
9. Performing Organization Name and Address NASA Langley Research Center Hampton, Va. 23365		10. Work Unit No. 124-07-23-01-23
		11. Contract or Grant No.
12. Sponsoring Agency Name and Address National Aeronautics and Space Administration Washington, D.C. 20546		13. Type of Report and Period Covered Technical Note
		14. Sponsoring Agency Code

15. Supplementary Notes

16. Abstract

Axial force, normal force, pitching moment, and ram- and static-pressure distributions were obtained on solid configurations representative of a supersonic decelerator concept. This concept utilizes an inflatable axisymmetric afterbody attached to the base of a 120° cone for drag augmentation and a burble fence located near the maximum diameter of the afterbody for subsonic stability. Two afterbody shapes were tested with burble fences that protruded above the surface as much as 20 percent of the afterbody maximum radius. Tests were also conducted to determine the feasibility of deploying an attached inflatable afterbody at supersonic speed. Aerodynamic forces were obtained at angles of attack up to 12° and at free-stream Reynolds numbers of 1.1×10^6 and 3.0×10^6. Ram and static pressures were obtained at 0° angle of attack and at a free-stream Reynolds number of 9.8×10^6. Inflatable models were tested at 0° angle of attack and at free-stream Reynolds numbers between 13.9×10^6 and 18.5×10^6 for ratios of afterbody volume to ram inlet area between 355 and 1167 inches (9.02 and 29.64 m). Reynolds numbers are based on maximum diameter of the afterbody.

17. Key Words (Suggested by Author(s)) Decelerator, Attached inflatable decelerator, Cones, Aerodynamic characteristics, Pressure distributions		18. Distribution Statement Unclassified – Unlimited	
19. Security Classif. (of this report) Unclassified	20. Security Classif. (of this page) Unclassified	21. No. of Pages 59	22. Price* $3.00

*For sale by the Clearinghouse for Federal Scientific and Technical Information Springfield, Virginia 22151

STATIC AERODYNAMIC CHARACTERISTICS, PRESSURE DISTRIBUTIONS, AND RAM-AIR INFLATION OF ATTACHED INFLATABLE DECELERATOR MODELS AT MACH 3.0

By William D. Deveikis and James Wayne Sawyer
Langley Research Center

SUMMARY

A wind-tunnel investigation was conducted to obtain static longitudinal aerodynamic characteristics and ram- and static-pressure distributions of solid configurations representative of a supersonic decelerator concept which utilized an inflatable axisymmetric afterbody attached to the base of a 120° cone for drag augmentation and a burble fence for subsonic stability. Data were obtained for two afterbody configurations with burble fences that protruded above the afterbody surface as much as 20 percent of the afterbody maximum radius. Tests were also conducted to determine the feasibility of supersonically deploying an inflatable afterbody with ram-air inlets located on the cone forebody. Axial force, normal force, and pitching moment were measured at angles of attack up to 12° and at free-stream Reynolds numbers of 1.1×10^6 and 3.0×10^6. Ram- and static-pressure distributions were obtained at 0° angle of attack and at a free-stream Reynolds number of 9.8×10^6. For the ram-inflation tests the angle of attack was 0°, the ratio of afterbody volume to inlet area was varied from 355 to 1167 inches (9.02 to 29.64 m), and free-stream Reynolds numbers were between 13.9×10^6 and 18.5×10^6. Reynolds numbers are based on afterbody maximum diameter.

Results from the tests on solid models without a burble fence indicated that the axial-force coefficient increased with increasing afterbody bluffness, whereas static stability decreased; however, the static stability was substantially greater than that of the 120° cone. The burble fence induced boundary-layer separation and could improve or degrade the static longitudinal aerodynamic characteristics, depending on the burble-fence height, shape, and location. Although all decelerator shapes generated axial-force coefficients considerably smaller than that of the 120° cone, the drag force exceeded that of the cone by factors between 2.0 and 5.8 as a result of the increase in projected frontal area by factors between 3.6 and 9.0 produced by the afterbodies.

Measured surface pressures increased with afterbody bluffness and were in disagreement with Newtonian values along the cone forebody and at the burble fence. Ram pressures exceeding stagnation-point values defined a region considered suitable for

the placement of ram-air inlets between the stagnation point and a location on the afterbody where the local Mach number was just above sonic. The ram-inflation tests showed that supersonic deployment of attached inflatable afterbodies by ram pressure is feasible at dynamic pressures between 1457 and 1704 pounds per square foot (70 and 82 kN/m^2). Afterbody internal pressure ranged from values that were approximately 2.5 percent less than stagnation-point pressure to local static pressure. As the ratio of afterbody volume to ram inlet area increased, afterbody inflation time increased and afterbody internal pressure decreased.

INTRODUCTION

Recent interest in the large-angle cone for use in supersonic decelerator systems has led to the evaluation of concepts which utilize an expandable afterbody for drag augmentation (refs. 1 and 2). One such concept is the attached inflatable decelerator illustrated in figure 1 and discussed in references 1 and 3. With this concept, the inflatable axisymmetric afterbody is attached to the cone base, and its shape is sustained by directing ram pressure through suitably placed inlets. The burble fence, shown near the maximum diameter of the afterbody, provides subsonic stability (ref. 3). Afterbody shapes are determined from the analysis of reference 3, which is based on the isotensoid shell theory of reference 4.

Previous experimental work on this concept has included free-flight and wind-tunnel tests on models with a flexible afterbody. These have provided data on subsonic and supersonic drag and static-stability characteristics, structural performance, and supersonic deployment characteristics, as reported in reference 3. Data are also available on supersonic drag and static-stability characteristics for a solid attached inflatable decelerator shape without a burble fence (ref. 5). The present investigation was undertaken to provide wind-tunnel data on supersonic drag, static stability, and surface pressure distributions for solid shapes with a burble fence. Other objectives were to obtain ram-pressure distributions to define favorable areas for the placement of ram-air inlets and to determine the feasibility of supersonically deploying an inflatable afterbody solely by means of ram pressure with ram-air inlets located on the cone forebody.

Aerodynamic forces and pressure distributions were obtained for solid models of two afterbody shapes attached to the base of a spherically blunted 120° cone with burble fences that protruded above the afterbody surface as much as 20 percent of the afterbody maximum radius. Aerodynamic forces were measured at angles of attack up to 12° and at free-stream Reynolds numbers, based on afterbody maximum diameter, of 1.1×10^6 and 3.0×10^6 on solid models 1.25 inches (3.10 cm) in diameter in the 9- by 6-inch model tunnel at the Langley Research Center. Ram- and surface-pressure distributions were

obtained on solid models 20 inches (51.80 cm) in diameter at 0° angle of attack and a free-stream Reynolds number, based on afterbody maximum diameter, of 9.8×10^6 in the Langley 9- by 6-foot thermal structures tunnel. This facility was also used for the ram-inflation tests which were conducted on models with an inflatable afterbody 25 inches (63.5 cm) in diameter at 0° angle of attack. Free-stream Reynolds numbers, based on afterbody maximum diameter, were between 13.9×10^6 and 18.5×10^6, and the ratio of afterbody volume to ram inlet area was varied from 355 to 1167 inches (9.02 to 29.64 m). The free-stream Mach number for all tests was 3.0.

SYMBOLS

Physical quantities in this paper are given both in the U.S. Customary Units and in the International System of Units (SI). Factors relating the two systems are given in reference 6, and those used in the present investigation are presented in the appendix.

A maximum cross-sectional area of model and burble fence, $\pi(r_b + h)^2$

A_r ram inlet area

C_A axial-force coefficient, $\frac{\text{Axial force}}{qA}$

C_D drag coefficient, $\frac{\text{Drag force}}{qA}$

C_m pitching-moment coefficient, $\frac{\text{Pitching moment}}{2qA(r_b + h)}$

C_{m_α} slope of the pitching-moment curve at zero angle of attack, per degree, $\left(\frac{\partial C_m}{\partial \alpha}\right)_{\alpha=0^{\circ}}$

C_N normal-force coefficient, $\frac{\text{Normal force}}{qA}$

C_{N_α} slope of the normal-force curve at zero angle of attack, per degree, $\left(\frac{\partial C_N}{\partial \alpha}\right)_{\alpha=0^{\circ}}$

C_p surface pressure coefficient, $\frac{p_l - p}{q}$

$C_{p,b}$	base-pressure coefficient, $\frac{p_b - p}{q}$
$d = 2r_b$	
h	burble-fence height (fig. 2)
k	Newtonian constant
M	free-stream Mach number
M_l	local Mach number
n	normal distance from the body surface
p	free-stream static pressure
p_b	model base pressure
p_i	afterbody internal pressure
p_l	local surface pressure
p_r	ram pressure
p_t	free-stream total pressure
q	free-stream dynamic pressure
R	Reynolds number based on afterbody maximum diameter d
r	radial coordinate (fig. 2(a))
r_b	maximum radius of afterbody (fig. 2(a))
r_c	base radius of cone forebody
r_n	radius of spherical nose

T	total temperature
t_f	afterbody fill time determined from motion pictures
t_i	time for afterbody internal pressure p_i to stabilize
V	afterbody volume
x	axial coordinate (fig. 2(a))
x'	axial coordinate measured from model nose
x_{ac}	axial coordinate of aerodynamic center, $2\left(r_b + h\right)\frac{C_{m_\alpha}}{C_{N_\alpha}}$
α	angle of attack

MODELS, APPARATUS, AND TESTS

Force-Test Models

Axial force, normal force, and pitching moment were measured on solid models of the configurations shown in figure 2, whose coordinates are given in table I. The body-axis system is shown in figure 2(a). The forebody of shape 1 was a spherically blunted $\left(r_n/r_b = 0.105\right)$ 120° cone, and the slope of the afterbody at the cone-afterbody juncture was less than that of the forebody. Shape 1 with the burble fence (fig. 2(b)) is representative of the large-scale subsonic-flight demonstration model of reference 3. Shape 2 was shorter and bluffer than shape 1. Its forebody was also a spherically blunted $\left(r_n/r_b = 0.080\right)$ 120° cone, but the slope of the afterbody at the cone-afterbody juncture was greater than that of the forebody. With respect to the forebody, afterbody shapes 1 and 2, excluding burble fences, increased the frontal area by factors of 3.6 and 6.3, respectively.

Shape 1 was tested with one burble fence; its coordinates are given in table I, and its maximum radius $r_b + h$ was $1.15r_b$. Thus, the total projected frontal area was 4.8 times that of the cone forebody. When attached to shape 1, the leading edge of the burble fence was located close to the circle generated by the afterbody maximum radius r_b. Shape 2 was tested with two burble fences whose longitudinal cross-sectional shape was a circular arc of radius h with its origin located at the circle generated by the afterbody maximum radius. The maximum radii of the burble fences were $1.10r_b$ and $1.20r_b$. Thus, the total projected frontal areas were 7.6 and 9.0 times that of the cone forebody.

The models were designed with detachable burble fences and were machined from stainless steel as simple bodies of revolution – that is, without the lobes that would form between the seams of an inflated afterbody made of fabric as illustrated in figure 1. The afterbodies were constructed without the base cavity, and the burble fences were machined as flat circular disks with shaped edges. For tests requiring the burble fence, the rear surface of the afterbody was cut to match the diameter of the front face of each burble-fence disk. Model base diameters were 1.25 inches (3.10 cm), and surfaces were polished to a finish of approximately 10 microinches (250 nm), rms.

Pressure-Distribution Models

Pressure distributions were obtained on solid models of the configurations shown in figure 3. The models and detachable burble fences were constructed of cherry wood with smooth, unlobed surfaces that were impregnated with an epoxy resin and then polished. Afterbody maximum radii (r_b) were 9.50 and 10.00 inches (24.13 and 25.40 cm) for shapes 1 and 2, respectively. The maximum radius $r_b + h$ of the burble fence for shape 1 was 10.93 inches (27.76 cm). For shape 2, the maximum radii of the burble fences were 11.00 and 12.00 inches (27.94 and 30.48 cm).

Static- and ram-pressure orifices were installed at the locations indicated in figure 3 and in tables II and III. For shape 1, static pressure was measured at 39 stations on the model surface and at seven stations on its burble fence; for shape 2, static pressure was measured at 33 stations on the model surface and at 10 stations on each burble fence. The static orifices were located in a plane containing the model axis. Ram pressure was measured along the surface of shapes 1 and 2 at four and seven stations, respectively. These orifices were located at a distance above the surface of 0.25 inch (0.64 cm) and were staggered circumferentially to avoid mutual interference. On shape 2 with the largest burble fence attached, ram pressures were also measured at seven stations along a normal to the cone-forebody surface at the cone base for distances up to 2 inches (5.08 cm) or $n = 0.2r_b$.

Ram-Inflation Models

Details of the ram-inflation models used in the present investigation are illustrated in figures 4 and 5. Two models of each type were constructed, and each model had a different ram inlet area. The ram inlet area of model B was approximately two-thirds that of model A (fig. 4), and the ram inlet area of model D was approximately one-half that of model C (fig. 5). The ram-air inlet ports shown in the figures were designed to allow rapid deployment of the afterbody and to maintain ram pressure in the afterbody. The inlet ports of the models of figure 4 were shielded from the airstream by a membrane cover. For these models, afterbody inflation was initiated by energizing a nichrome wire

(see detail A and view BB of fig. 4) which burned through the membrane cover around three edges of each port and thus permitted introduction of ram air into the afterbody. For the models of figure 5, afterbody inflation was initiated by retracting a portion of the cone forebody to the position shown. The movable portion of the cone was connected to the fixed portion by means of an explosive bolt not shown in the figure. When the explosive bolt was detonated, the dynamic pressure of the airstream forced the movable portion rearward.

The inflatable afterbodies were fabricated from nylon twill fabric which was coated with neoprene on both sides. The afterbodies were designed to have a maximum diameter of 25 inches (63.5 cm) and to assume shape 2 (fig. 2(c)) upon inflation. Afterbody volumes were estimated to be 3500 cubic inches (0.0574 m^3) for the models of figure 4 and 3477 cubic inches (0.0570 m^3) for the models of figure 5. An afterbody was formed by joining 28 pieces of fabric cut on the bias, using double-strap butt joints and double meridional cords at the seams as shown in view AA of figure 4. All joints were cemented with a contact rubber-base cement. Each afterbody was cemented to the inlet ring located at the base of the cone forebody and was clamped between fittings at the rear attachment. Tiedown tabs were provided to secure the afterbody to the sting.

Pertinent afterbody material data are as follows:

Material thickness: 0.008 inch (0.020 cm)

Material mass: 7.38 ounces per square yard (0.25 kg/m^2)

Fabric mass (uncoated): 5 ounces per square yard (0.17 kg/m^2)

Pull strength of material in the weave direction: 160 pounds per inch (28 kN/m)

Meridional cord strength: 120 pounds (533 N), rated

Instrumentation

Pressures were measured with the aid of strain-gage pressure transducers connected to orifice tubes installed in the pressure-distribution and ram-inflation models. On the ram-inflation models, the diaphragm of a transducer was mounted flush with the rear surface of the inlet ring to sense the afterbody internal pressure, and ram pressure was measured by means of an orifice tube installed in one of the inlet ports. (See figs. 4 and 5.) Aerodynamic forces and pitching moments acting on the force-test models were measured with the aid of an externally mounted, three-component, strain-gage sting-balance assembly which was shielded from the airstream by means of a shroud. An orifice tube, attached to the outer surface of the sting-balance shroud and located in the yaw plane, was used for measuring model base pressure. The output from the transducers and the strain-gage balance was recorded and reduced to useful form at the

Langley central digital recording facility. In the aerodynamic-forces tests, angle of attack was indicated by a digital voltmeter that recorded the output from a linear potentiometer attached to an angle-of-attack mechanism on which the model-sting-balance system was mounted. Flow angularity and sting deflection due to air loads were not taken into account in the angle-of-attack readings, but static load calculations showed that the sting deflection should not have exceeded 0.3°. Shock waves and flow patterns generated by the force-test models were recorded photographically with the aid of a single-pass horizontal Z-light-path schlieren system and a spark light source of approximately 0.2-microsecond duration. High-speed motion-picture photography was used to record events during the ram-inflation tests.

Test Facilities

The pressure-distribution and ram-inflation models were tested in the Langley 9- by 6-foot thermal structures tunnel, whereas the force-test models were tested in the 9- by 6-inch model tunnel at the Langley Research Center. Both facilities are blowdown wind tunnels which operate at a Mach number of 3.0 with less than 1 percent deviation, at stagnation pressures between 50 and 200 pounds per square inch (345 to 1380 kN/m^2) absolute over a stagnation-temperature range between ambient and 2000° F (1360 K), and use the same air supply. Other details on these facilities may be found in reference 7.

Model Mounting

Force-test models.- The model-sting configuration for the aerodynamic-forces tests conducted in the 9- by 6-inch model tunnel is illustrated in figure 6. At the model base, the ratio of the sting-balance shroud diameter to the maximum diameter of the model afterbody was 0.44. At a distance 4d downstream of the model base, the sting-balance shroud flared outward at 14.5° to increase the ratio to 1.2.

Pressure-distribution models.- The pressure-distribution models were sting mounted and fixed at 0° incidence with respect to the tunnel center line. The model-sting configuration for these models is illustrated in figure 7. At the model base the ratio of the sting diameter to the maximum diameter of the model afterbody was 0.12. At a distance 0.7d downstream of the model base, the sting flared outward at 15° to increase the ratio to 0.24. A cruciform sting mount was located approximately three model diameters downstream of the model base. Front and rear views of a typical pressure-distribution-model test setup in the Langley 9- by 6-foot thermal structures tunnel are shown in figures 8 and 9.

Ram-inflation models.- The ram-inflation models were mounted and fixed at 0° incidence with respect to the tunnel center line on the same sting configuration that was used in the pressure-distribution-model tests. The afterbody was folded tightly behind

the cone forebody as shown in figure 10 and was secured by cords looped through the tiedown tabs and around a tiedown cord that was wrapped around the sting. To release the afterbody, an electrically actuated cutter was used to sever the tiedown cord.

Tests

Aerodynamic-forces tests.- Aerodynamic forces and pitching moments were measured at angles of attack up to 12° in tests conducted at ambient stagnation temperatures and at stagnation pressures of 65 to 170 pounds per square inch (448 to 1170 kN/m^2) absolute. Reynolds numbers, based on afterbody maximum diameter $2r_b$, were approximately 1.1×10^6 and 3.0×10^6. The test procedure was to start the tunnel with the model oriented at zero angle of attack. After flow conditions had stabilized in the test section, data were recorded at the low and then at the high stagnation-pressure level at each angle of attack for 5 seconds to insure an equilibrium base-pressure response. Prior to terminating a test, data were recorded a second time at 1° and at -1° angle of attack to determine whether shifts in the balance output had occurred. No data were acquired during the change from one angle of attack to another.

Pressure-distribution tests.- The pressure-distribution tests were conducted at a stagnation temperature of approximately 250° F (395 K) and a stagnation pressure of 60 pounds per square inch (414 kN/m^2) absolute. The corresponding free-stream Reynolds number, based on afterbody maximum diameter $2r_b$, was approximately 9.8×10^6. Test duration was approximately 30 seconds to provide sufficient time for the pressures sensed by the transducers to reach equilibrium. Except for shape 1 with the burble fence attached, all configurations were tested twice at the same test conditions. For the repeat test, the transducers were interchanged.

Ram-inflation tests.- Just prior to testing, the internal pressure of the model was reduced to approximately 1 pound per square inch (7 kN/m^2) absolute by means of a vacuum pump and was maintained at this pressure until the introduction of ram air. In tests of models A and B, the electrical circuits to the nichrome wire around the inlet ports and the cutter were energized simultaneously. However, because of the thermal inertia of the membrane burning system, inflation began approximately 0.3 second after the tiedown cord was severed. In tests of models C and D, a time-delay relay was installed in the circuitry which released the retractable portion of the cone forebody approximately 0.1 second after the tiedown cord was severed. The tests were conducted over a range of stagnation pressures between 59 and 69 pounds per square inch (407 and 476 kN/m^2) absolute. Corresponding free-stream dynamic pressures were between 1457 and 1704 pounds per square foot (70 and 82 kN/m^2). Stagnation temperatures did not exceed 200° F (367 K), and free-stream Reynolds numbers, based on afterbody maximum diameter $2r_b$, were between 13.9×10^6 and 18.5×10^6.

Data

The aerodynamic data were resolved about the body-axis system shown in figure 2(a). The following are estimated accuracies based on 1 percent of full-scale deflection for pressures and 0.5 percent of full load for each balance component:

	$R \approx 1.1 \times 10^6$	$R \approx 3.0 \times 10^6$
C_p	±0.025	±0.025
C_A	±0.024	±0.008
C_m	±0.010	±0.004
C_N	±0.008	±0.002

In addition to the above tolerances on the strain-gage balance data, a zero shift in the balance output was encountered between no-flow and flow conditions which often led to nonzero pitching-moment and normal-force coefficients at $\alpha = 0^{\circ}$. The cause of the balance output shift has not been isolated, but data obtained at $\alpha = \pm 1^{\circ}$ at the beginning and near the end of a test showed excellent repeatability for all models. Consequently, since the balance sensitivity apparently did not change during the tests, the slopes of the C_m and C_N variations with α used in evaluating C_{m_α} and C_{N_α} are considered valid.

RESULTS AND DISCUSSION

Flow Patterns

Typical flow patterns associated with the attached inflatable decelerator shapes 1 and 2 are shown in the schlieren photographs of figures 11 and 12. The photographs were taken with the models oriented at $\alpha = 0^{\circ}$ and 12° for Reynolds numbers of 1.1×10^6 and 3.0×10^6. The results show that all configurations generated a detached bow shock wave whose local slope and standoff distance increased with increasing body bluffness as seen, for example, by comparing the photographs of shapes 1 and 2 without the burble fence. For shape 1, the burble fence had little effect on the shock-wave profile and standoff distance, but for shape 2, the bluffness of the shock-wave profile and the shock-wave standoff distance increased with increasing burble-fence size. Without the burble fence, the flow around both shapes appeared relatively undisturbed. With the burble fence attached, boundary-layer flow separation occurred ahead of the fence, and the location of the separation point at $\alpha = 0^{\circ}$, as determined from the schlieren negatives and indicated by the white arrowheads, moved upstream with increasing burble-fence size. When the models were displaced to other angles of attack, the location of the separation point moved upstream along the upper surface and downstream along the lower surface as shown by the white arrowheads in the photographs for $\alpha = 12^{\circ}$. Increasing the Reynolds number from 1.1×10^6 to 3.0×10^6 produced no significant change in the location of the separation point.

The shock wave emanating from the boundary-layer separation point ahead of the burble fence on shape 1 indicates the presence of locally supersonic velocities. Similar but weaker disturbances were also observed in the schlieren negatives for shape 2 with its smaller burble fence attached $\left(h/r_b = 0.10\right)$.

Aerodynamic Characteristics

All axial-force data obtained with the strain-gage balance have been corrected to a free-stream static-pressure condition at the model base. The specific corrections applied are presented as base-pressure coefficients in figure 13. All values are between 0.10 and 0.13. Thus, these measurements bracket the parameter $1/M^2$ often used as a base-pressure correction factor.

Variations of the pitching-moment, axial-force, and normal-force coefficients with angle of attack at $R \approx 1.1 \times 10^6$ and 3.0×10^6, obtained with the force-test models of decelerator shapes 1 and 2 (fig. 2), are presented in figures 14 and 15. It should be noted that these variations could differ for decelerators with a flexible afterbody because of the tendency of the afterbody to orient its axis parallel to the airstream when the cone forebody is displaced at an angle of attack. (See ref. 3.) Data from reference 8 are also shown for a 120° cone. All coefficients are based on the total projected frontal area of each configuration.

The coefficients showed only small Reynolds number effects. Over the present range of α, the pitching-moment coefficients increased negatively, the axial-force coefficients remained nearly constant, and the normal-force coefficients increased positively. The highest C_A values were obtained from the bluffer models (shape 2), but the effects of the burble fences on C_A were inconsistent in that C_A decreased when the burble fence was attached to shape 1 and increased with increasing burble-fence size on shape 2. The axial-force coefficients were substantially less for the decelerator shapes than for the 120° cone, but as shown in table IV, the drag force of the decelerator shapes was from 2 to 6 times greater than that of the 120° cone.

The slopes of the pitching-moment and normal-force coefficient curves at $\alpha = 0^{\circ}$ yielded the values of the parameters C_{m_α}, C_{N_α}, and $x_{ac}/2r_c$ shown as bar graphs in figure 16. The negative values of the stability parameter C_{m_α} indicate that all configurations were statically stable. Both shapes 1 and 2 without burble fences showed substantially larger values of C_{m_α} and C_{N_α} than the 120° cone, but the largest values were given by shape 1. When the burble fence was attached to shape 1 the values increased, but for shape 2, as was observed at subsonic speeds in reference 3, C_{m_α} and C_{N_α} increased when the smaller burble fence $\left(h/r_b = 0.10\right)$ was attached and then decreased to approximately the values of the 120° cone when the larger burble fence

$\left(h/r_b = 0.20\right)$ was attached. Thus, the static aerodynamic characteristics can either be improved or degraded by a burble fence.

The values of $x_{ac}/2r_c$ shown in figure 16 indicate that the aerodynamic centers of shapes 1 and 2 were located from approximately 0.75 to 1.55 cone-forebody diameters downstream of the 120° cone-forebody base. Distances to the aerodynamic center were greatest for the models with the burble fence attached. The downstream shift in the aerodynamic-center location relative to that of the 120° cone ranged from approximately 0.20 to 0.40 cone-forebody diameter for shape 1 and from approximately 0.70 to 0.98 cone-forebody diameter for shape 2.

Mach Number Distributions

Surface Mach numbers were evaluated at $\alpha = 0^{\circ}$ from the ratio of local static pressure to local total pressure obtained from the measured static and ram pressures. (See fig. 17.) These Mach numbers confirmed that the flow accelerated to supersonic values on the afterbody of both shapes. As indicated by the shaded portion of the sketches, the surface area covered by subsonic flow increased with increasing body bluffness. The location of the sonic point did not change on shape 1 when the burble fence was attached or on shape 2 when the smaller burble fence $\left(h/r_b = 0.10\right)$ was attached. However, when the larger burble fence $\left(h/r_b = 0.20\right)$ was attached to shape 2, the level of the local Mach numbers decreased over the area covered by the ram-pressure orifices, and the trend of the data suggests that the flow was subsonic on the entire surface upstream of the fence.

Pressure Distributions

Ram pressures.- Measured ram pressures, nondimensionalized with respect to the free-stream dynamic pressure, are presented in figure 18 as functions of the body radial coordinate and the distance normal to the surface. The data of figures 18(a) and 18(b) indicate that high ram pressures, about twice the value of the dynamic pressure, occurred in a region surrounding the body between the stagnation point and a location on the afterbody where the local Mach number is just above sonic. (Refer to the local Mach number distributions of fig. 17.) Figure 18(c) shows high ram pressures out to a value of $n/r_b = 0.20$ at $r/r_b \approx 0.4$. These high values are probably attainable out to the detached bow shock wave. Within the region downstream of the location where the local supersonic Mach numbers are high enough to sustain a detached shock wave ahead of the ram orifices, the ram pressures were substantially reduced as a result of normal-shock losses. (See, for example, values of p_r/q indicated by the circle symbols for the ram-orifice locations at $r/r_b = 1.03$ in fig. 18(a) and at $r/r_b = 1.02$ in fig. 18(b).) Thus, the shock-interference-free, high-ram-pressure region ahead of the sonic line between the surface and the bow shock wave appears best suited for the placement of ram-air inlets.

Surface pressures.- Surface pressure-coefficient distributions, as determined from experiment and from Newtonian and modified Newtonian theories, are presented as a function of body radial coordinate in figures 19 and 20 for shapes 1 and 2, respectively. Also indicated are the radial coordinates locating the cone-afterbody juncture and the burble-fence leading edge. In general, the repeatability of the measured data was excellent, usually within a C_p increment of 0.01. Except in the region of the cone-afterbody juncture, the experimental pressure distributions obtained from shapes without the burble fence (figs. 19(a) and 20(a)) are characterized by a negative pressure gradient along the front face and a relatively constant pressure less than free-stream static along the base. On shape 1 (fig. 19(a)), the decrease in the surface slope at the cone-afterbody juncture resulted in a local overexpansion of the flow downstream of the juncture followed by a compensating recompression of the flow as shown by the wriggle in the C_p data near $r/r_b = 0.6$. On shape 2, the pressure gradient approached zero at the cone-afterbody juncture, and pressures were higher along the front face than on shape 1. The higher surface pressures on shape 2 account for the bluffer shock-wave profiles and the greater standoff distances noted in the discussion of the schlieren photographs of the force-test models of figures 11 and 12.

For the models with the burble fence attached, the surface pressures increased just upstream of the burble fence, reached a peak value on the front face of the burble fence, and then decreased rapidly to the base-pressure level, as shown in figures 19(b), 20(b), and 20(c). The increase in surface pressure is associated with the boundary-layer flow separation observed in the schlieren photographs of figures 11 and 12. It is assumed herein that the location of the boundary-layer separation point is just upstream of the orifice that indicates the pressure rise and that the separated boundary layer reattached on the front face of the burble fence near the orifice indicating the peak pressure value. Time variations of the pressure-transducer output from orifices located under the separated boundary layer indicated a stable location of the separation point on both shapes 1 and 2. The rapidly decreasing surface pressure downstream of the peak pressure denotes attached, expanding flow around the burble-fence profile. No influence of afterbody shape or of burble-fence size and shape on the base-pressure level is indicated.

The Newtonian and the modified-Newtonian theoretical pressure distributions approximate the trend of the experimental surface-pressure data along the afterbody and along the burble fence where the boundary-layer flow was attached but show poor agreement with the test data along the cone forebody. Moreover, the theories are inherently insensitive to the effects of boundary-layer flow separation and other flow anomalies and, hence, show poor agreement with experiment along the surface under the separated boundary layer and in the vicinity of the cone juncture.

Effects of the burble fence on surface pressures.- A comparison of the data of figures 19(a) and 19(b) and of figures 20(a) and 20(b) shows that the presence of the burble fence on shape 1 and of the smaller burble fence $\left(h/r_b = 0.10\right)$ on shape 2 did not affect the surface pressures ahead of the boundary-layer flow separation point. However, substantially higher surface pressures were obtained over the front face of shape 2 with the larger burble fence $\left(h/r_b = 0.20\right)$.

This effect can be explained with the aid of figure 21, which shows sketches of the models with separated boundary layers and corresponding longitudinal pressure distributions. As shown in figures 21(b) and 21(d), the boundary-layer separation point was located downstream of the sonic point on shape 1 and on shape 2 with the burble fence for $h/r_b = 0.10$. Thus, flow disturbances were not transmitted upstream, and pressures ahead of the boundary-layer separation point were the same as those obtained without the burble fence. With the larger burble fence $\left(h/r_b = 0.20\right)$ on shape 2 (fig. 21(e)), the boundary-layer separation point was located upstream of the sonic point indicated for shape 2 in figures 21(c) and 21(d). The high level of surface pressures shown for this configuration indicates that the flow remained subsonic over the entire front face of the afterbody and expanded through a sonic point on the front face of the burble fence. These results suggest that a limiting burble-fence size probably exists for which the surface pressures ahead of the boundary-layer separation point will remain unaffected provided that the separation point lies downstream of the sonic point.

Separated boundary layer.- In addition to showing the separated boundary layers as determined from the experimental pressure distributions, figure 21 shows the boundary-layer separation points as determined from the schlieren photographs of the force-test models. For shape 1, the separation point on the force-test model is located slightly upstream of the separation point obtained on the pressure-distribution model. For shape 2, the separation point is located at approximately the same station on the force-test and pressure-distribution models; thus, an order-of-magnitude change in the Reynolds number resulting from the difference in model sizes had little effect on the location of the boundary-layer separation point. The reattachment points of the boundary layer on the burble fences indicate that the separated boundary layer of shape 1 masked the largest percentage of the front face of a burble fence.

Effects of the burble fence on integrated drag coefficient.- Drag coefficients at $\alpha = 0^{\circ}$, determined by integrating the experimental pressure distributions of figures 19 and 20, are presented in table V. Also shown are values obtained from the force-test models and from Newtonian theory. The drag coefficients obtained from the pressure distributions agree with those obtained from the aerodynamic-force tests and thus indicate the same effects of afterbody shape and burble-fence size that were observed in the force-test data – namely, that the drag coefficient of shape 2 was higher than that of

shape 1 and that the drag coefficient decreased when the burble fence was attached to shape 1 but increased with increasing burble-fence size on shape 2.

The sketches of figure 21 suggest that the factors which affect the drag coefficient when the burble fence is attached may be those which affect the separated boundary layer, such as the burble-fence size, shape, and location. For example, although the burble fence for shape 1 was larger than the smallest fence for shape 2, its profile was not as bluff. Furthermore, its leading edge was located near the afterbody maximum radius, whereas for shape 2 the burble-fence leading edges were located upstream of the afterbody maximum radius. Thus, the surface slope at the boundary-layer reattachment point on the burble fence of shape 1 was much less than at the reattachment point on the burble fences of shape 2. Hence, the flow-turning angle on shape 1 after boundary-layer reattachment was probably less than that required to decelerate the flow to subsonic velocities as occurred on shape 2 with the smaller fence. Therefore, the surface pressures were not sufficiently high to offset the effect on the drag coefficient of the increased frontal area due to the burble fence, with the result that the drag coefficient of shape 1 was less with the burble fence than without it.

A comparison of the drag coefficients determined from the experimental pressure distributions with those given by Newtonian ($k = 2.000$) and modified-Newtonian ($k = 1.755$) theories in table V shows that in spite of the discrepancies between the experimental and theoretical pressure distributions indicated in figures 19 and 20, the agreement in some instances is good, especially with the modified-Newtonian theory. The Newtonian values are higher than experiment by 5 to 28 percent, whereas the modified-Newtonian values are approximately 1 to 11 percent higher than experiment. The agreement between experiment and modified-Newtonian theory improves with increasing burble-fence height for shape 2. However, unlike the experimental data for shape 1, the theoretical values show an increase in drag coefficient with increasing burble-fence size for both shapes.

Ram-Inflation Tests

The ram-inflation tests demonstrated that an inflatable afterbody attached to the base of a large-angle cone can be supersonically deployed at high dynamic pressures solely by ram inflation. Motion pictures of the ram-inflation tests showed that inflation of the afterbody was rapid and symmetrical and was characterized by a pulsating motion which increased in frequency with time in both the longitudinal and radial directions until a stable afterbody shape was attained. The behavior of the afterbody during a portion of the inflation period is illustrated in figure 22 by motion-picture frames showing a side view of the model.

Side and rear views of two fully inflated models are presented in figure 23. As shown by the side views (figs. 23(a) and 23(b)), the afterbody shapes of both models differ from that of shape 2 (fig. 2(c)). The most obvious difference is that the slope at the forebody juncture, rather than being greater than that of the cone, as in figure 2(c), appears equal to that of the cone. Measurements taken from the photographs indicate that the maximum diameter of the inflated afterbody was slightly larger than the design value of 25 inches (64 cm).

Analysis of the motion pictures and pressure data yielded the inflation times and afterbody internal pressures listed in table VI. The results indicated that from the start of inflation, all models assumed a stable shape within 0.14 second and that the afterbody internal pressure reached equilibrium within 0.20 second. For the models equipped with membrane-covered inlets, all inlet ports were opened in approximately 0.015 second, whereas for the models with the retractable nose cone, the inlet was fully opened in approximately 0.005 second. As the ratio of afterbody volume to ram inlet area increased, inflation time increased and afterbody internal pressure decreased. A comparison of the afterbody internal pressures of table VI with the ram pressures of figure 18 shows that the afterbody internal pressures were substantially less than the ram pressures obtained on the pressure-distribution models. These lower pressures are attributable to the inlet configurations of the ram-inflation models and to possible porosity of the afterbodies. For the smallest value of V/A_r (model A), the afterbody internal pressure was 2.5 percent less than the stagnation-point value shown in figure 18. For the largest value of V/A_r (model D), the afterbody internal pressure, $p_i/q = 1.77$, approximated the local static pressure on the cone forebody of the pressure-distribution model of shape 2 at a location corresponding to that of the ram inlet on the inflatable models. $\left(\text{Add } p/q = 0.16 \text{ for } M = 3.0 \text{ to estimated } C_p \approx 1.62 \text{ at } r/r_b = 0.26 \text{ in fig. 21(a) to obtain } p_l/q = 1.78.\right)$

CONCLUSIONS

A wind-tunnel investigation was conducted at a Mach number of 3.0 to obtain static longitudinal aerodynamic characteristics and ram- and static-pressure distributions of solid configurations representative of a supersonic decelerator concept which utilized an inflatable axisymmetric afterbody attached to the base of a 120° cone for drag augmentation and a burble fence for subsonic stability. Data were obtained for two afterbody shapes with burble fences that protruded above the afterbody surface as much as 20 percent of the afterbody maximum radius. Tests were also conducted to determine the feasibility of supersonically deploying an inflatable afterbody with ram-air inlets located on the cone forebody. The results indicated the following conclusions:

1. All decelerator shapes were statically stable.

2. For shapes without a burble fence, axial-force coefficient increased with increasing afterbody bluffness, but static stability and normal-force-curve slope C_{N_α} decreased; however, these shapes showed substantially greater static stability and C_{N_α} than the 120° cone.

3. A burble fence induces boundary-layer flow separation and can either improve or degrade the static stability, C_{N_α}, and axial-force coefficient depending on the burble-fence height, shape, and location.

4. The axial-force coefficients of the decelerator shapes were considerably less than that of the 120° cone, but their drag forces were from 2.0 to 5.8 times greater than that of the cone because of the increase in projected frontal area by factors between 3.6 and 9.0 produced by the afterbodies.

5. Aerodynamic-center locations of the decelerator shapes varied between approximately 0.20 and 1 cone-forebody diameter downstream of the aerodynamic-center location of the 120° cone.

6. A limiting burble-fence size probably exists for which the surface pressures ahead of the boundary-layer flow separation point will remain unaffected provided that the separation point lies downstream of the sonic point.

7. Newtonian pressure distributions yielded drag coefficients from 5 to 28 percent greater than the drag coefficients obtained by integrating the experimental pressure distributions; the deviation of modified-Newtonian drag coefficients from experimental values was between 1 and 11 percent.

8. Measured ram pressures exceeding stagnation-point values defined a region considered suitable for the placement of ram-air inlets between the stagnation point and a location on the afterbody where the local Mach number was just above sonic.

9. Supersonic deployment of attached inflatable afterbodies by ram pressure is feasible at high dynamic pressures with ram-air inlets located on the cone forebody; however, the afterbody internal pressure was less than the ram pressure measured on the solid models and varied from a value that was approximately 2.5 percent less than stagnation-point pressure to a value equal to the local static pressure.

10. As the ratio of afterbody volume to ram inlet area increased, afterbody inflation time increased and afterbody internal pressure decreased.

Langley Research Center,
National Aeronautics and Space Administration,
Hampton, Va., March 16, 1970.

APPENDIX

CONVERSION OF U.S. CUSTOMARY UNITS TO SI UNITS

Physical quantity	U.S. Customary Unit	Conversion factor (*)	SI Unit (**)
Length	in.	0.0254	meter (m)
Pressure	psi	6.895×10^3	newton/meter^2 (N/m^2)
Temperature	^{o}F	(5/9)(^{o}F + 460)	Kelvin (K)

*Multiply value given in U.S. Customary Unit by conversion factor to obtain equivalent value in SI Unit.

**Prefixes to indicate multiples of units are as follows:

Prefix	Multiple
kilo (k)	10^3
centi (c)	10^{-2}
nano (n)	10^{-9}

REFERENCES

1. Guy, L. D.: Structural Design Options for Planetary Entry. AIAA Paper No. 68-344, Apr. 1968.
2. Sawyer, James Wayne; and Deveikis, William D.: Effects of Modifications to Bluff Tension Shell Shapes on Aerodynamic Characteristics at Mach 3.0. NASA TM X-1949, 1970.
3. Mikulas, Martin M., Jr.; and Bohon, Herman L.: Development Status of Attached Inflatable Decelerators. J. Spacecraft Rockets, vol. 6, no. 6, June 1969, pp. 654-660.
4. Houtz, N. E.: Optimization of Inflatable Drag Devices by Isotensoid Design. AIAA Paper No. 64-437, June-July 1964.
5. Davenport, Edwin E.: Static Longitudinal Aerodynamic Characteristics of Some Supersonic Decelerator Models at Mach Numbers of 2.30 and 4.63. NASA TN D-5219, 1969.
6. Comm. on Metric Pract.: ASTM Metric Practice Guide. NBS Handbook 102, U.S. Dep. Com., Mar. 10, 1967.
7. Schaefer, William T., Jr.: Characteristics of Major Active Wind Tunnels at the Langley Research Center. NASA TM X-1130, 1965.
8. Deveikis, William D.; and Sawyer, James Wayne: Effects of Cone Angle, Base Flare Angle, and Corner Radius on Mach 3.0 Aerodynamic Characteristics of Large-Angle Cones. NASA TN D-5048, 1969.

TABLE I.- AFTERBODY COORDINATES

Shape 1

x/r_b	r/r_b	x/r_b	r/r_b
0	0.526	0.954	0.941
.007	.538	.980	.911
.033	.572	1.006	.877
.059	.604	1.033	.832
.085	.633	1.059	.755
.112	.660	1.059	.622
.138	.686	1.033	.540
.164	.709	1.006	.489
.191	.735	.980	.444
.217	.757	.954	.406
.243	.780	.928	.370
.270	.799	.901	.340
.296	.819	.875	.313
.322	.837	.849	.286
.349	.854	.822	.262
.375	.870	.796	.244
.401	.885	.773	.225
.428	.900	.743	.209
.454	.911	.717	.194
.480	.923	.691	.181
.517	.934	.664	.169
.533	.944	.638	.160
.559	.954	Burble fence	
.585	.962	0.805	1.000
.612	.970	.841	1.099
.638	.977	.878	1.131
.664	.985	.914	1.146
.691	.990	.950	1.151
.717	.995	.987	1.145
.743	.998	1.023	1.127
.773	.999	1.060	1.078
.796	1.000	1.067	1.050
.822	.998	1.060	1.023
.849	.995	1.023	.982
.875	.987	.987	.963
.901	.976	.950	.956
.928	.961	.914	.966

Shape 2

x/r_b	r/r_b	x/r_b	r/r_b
0	0.399	0.658	0.983
.009	.421	.683	.973
.034	.474	.708	.959
.059	.530	.732	.942
.084	.577	.757	.922
.108	.622	.782	.895
.133	.665	.807	.861
.158	.708	.832	.813
.183	.747	.857	.683
.208	.783	.832	.554
.233	.814	.807	.498
.258	.846	.782	.456
.283	.874	.757	.420
.308	.897	.732	.390
.333	.919	.708	.365
.358	.938	.683	.342
.383	.952	.658	.321
.408	.964	.633	.303
.433	.975	.608	.285
.458	.983	.583	.268
.483	.991	.558	.256
.508	.997	.533	.243
.533	.998	.508	.229
*.558	*1.000	.483	.218
.583	.997	.458	.207
.608	.994	Burble fences:	
.633	.989	$h/r_b = 0.10$	
		$h/r_b = 0.20$	

*Center of circular arc defining longitudinal cross-sectional shape of burble fences.

TABLE II.- STATIC-PRESSURE ORIFICE LOCATIONS

Static-pressure orifice locations, r/r_b, for –			
Shape 1		Shape 2	
0	[c]0.791	0	Burble fence, $h/r_b = 0.10$
.076	[b].827	.097	
.164	[c].862	[b,c].197	[c]1.000
[a].177	.896	[a].298	1.026
[b].253	[c].928	.301	[c]1.050
[a].266	.958	.373	1.071
.345	.974	[c].399	[c]1.087
[a].402	[b,c].988	.424	1.097
[b].436	1.000	[b,c].501	1.100
.483	Burble fence, $h/r_b = 0.15$	[c].580	Burble fence, $h/r_b = 0.20$
.504		[c].654	
[c].526	[c]1.046	[c].719	[c]1.000
.553	[c]1.101	[b,c].778	1.052
.579	1.155	[c].835	[c]1.100
[b,c].626	[a].985	[c].889	1.141
.672	[a].959	[c].938	[c]1.732
[c].714		[b,c].984	1.932
.753		1.000	1.200

[a]Back face.

[b]Two orifices 180° apart, front face only.

[c]Front and back faces.

TABLE III.- RAM-PRESSURE ORIFICE LOCATIONS

Ram-pressure orifice locations for –				
Shape 1 Along the surface		Shape 2		
		Along the surface		Normal to the surface, n/r_b
x'/r_b	r/r_b	x'/r_b	r/r_b	
0.128	0.311	0.190	0.404	0.015
.335	.636	.234	.499	.025
.578	.849	.283	.601	.050
1.045	1.025	.340	.696	.075
		.404	.800	.100
		.490	.899	.150
		.767	1.023	.200

TABLE IV.- DRAG FORCE OF DECELERATOR MODEL

RELATIVE TO DRAG FORCE OF 120° CONE

Reynolds number	$\frac{(C_DA)_{deployed}}{(C_DA)_{undeployed}}$ at constant q for –				
	Shape 1		Shape 2		
	$h/r_b = 0$	$h/r_b = 0.15$	$h/r_b = 0$	$h/r_b = 0.10$	$h/r_b = 0.20$
1.1×10^6	2.17	1.97	4.94	5.38	5.82
3.0×10^6	2.19	2.02	4.97	5.36	5.70

TABLE V.- DRAG COEFFICIENTS

Model shape	Burble-fence height, h/r_b	C_D at $\alpha = 0^o$ from –				
		Force-test models		Pressure-distribution models, $R \approx 9.8 \times 10^6$	Newtonian theory	
		$R \approx 1.1 \times 10^6$	$R \approx 3.0 \times 10^6$		$k = 2.000$	$k = 1.755$
1	0	0.871	0.856	0.873	0.920	0.810
1	.15	.811	.792	.790	1.000	.880
2	0	1.136	1.123	1.121	1.350	1.180
2	.10	1.230	1.210	1.172	1.395	1.225
2	.20	1.330	1.300	1.319	1.483	1.302

TABLE VI.- RAM-INFLATION TEST CONDITIONS AND RESULTS

Model	Ram inlet type	A_r	V/A_r	T	p_t	R	q	p_i/q	t_i, sec	t_f, sec
A	Membrane covered	9.87 in^2 (63.68 cm^2)	355 in. (9.02 m)	200° F (367 K)	59 psia (407 kN/m^2)	13.9×10^6	1457 psf (70 kN/m^2)	1.87	No data return	0.10
B	Membrane covered	6.58 in^2 (42.45 cm^2)	532 in. (13.51 m)	200° F (367 K)	61 psia (421 kN/m^2)	14.1×10^6	1506 psf (72 kN/m^2)	1.84	No data return	0.12
C	Retractable nose cone	5.88 in^2 (37.94 cm^2)	591 in. (15.01 m)	200° F (367 K)	63 psia (434 kN/m^2)	14.6×10^6	1556 psf (74 kN/m^2)	1.82	0.13	0.11
D	Retractable nose cone	2.98 in^2 (19.23 cm^2)	1167 in. (29.64 m)	150° F (339 K)	69 psia (476 kN/m^2)	18.5×10^6	1704 psf (82 kN/m^2)	1.77	0.20	0.14

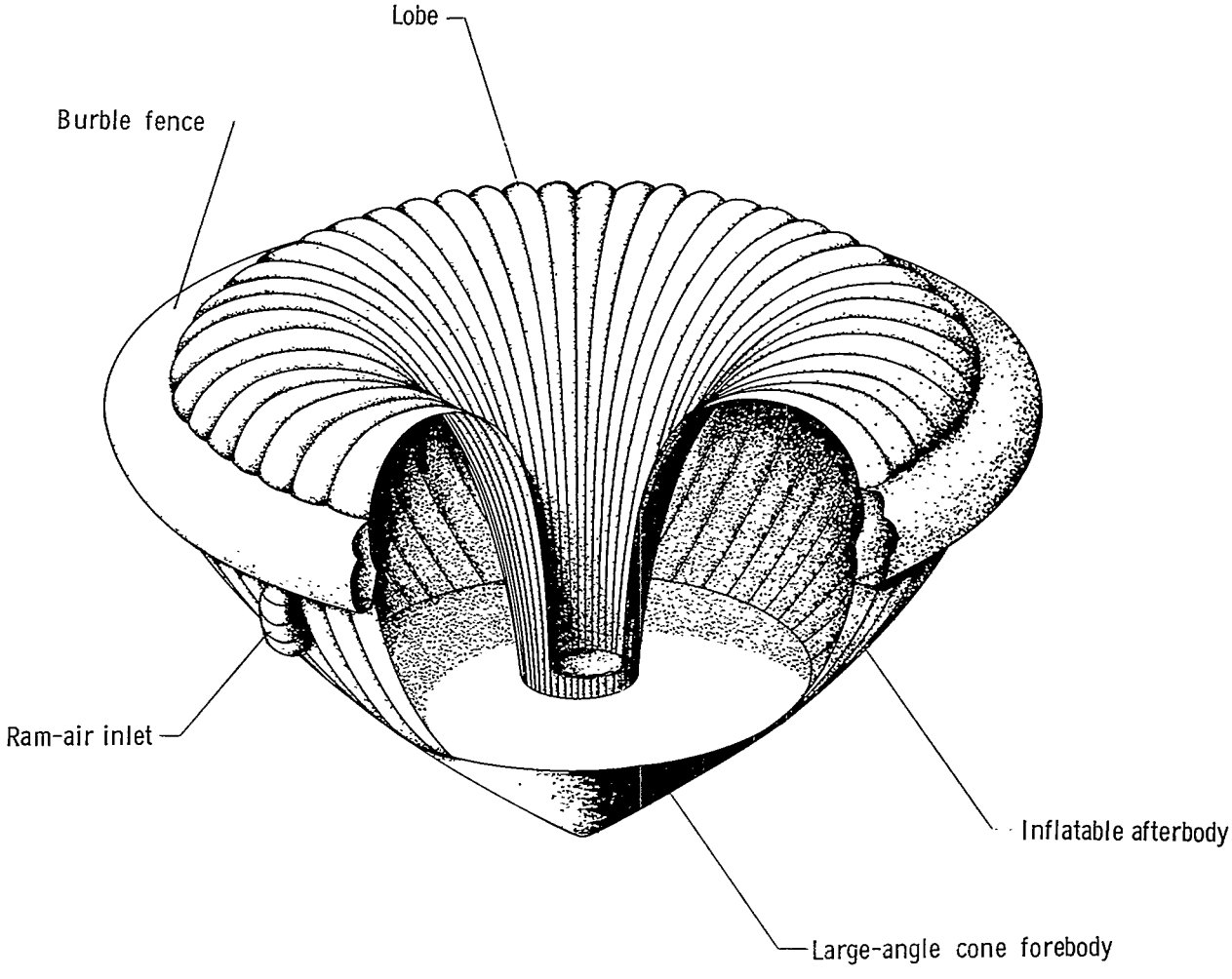

Figure 1.- Illustration of an attached inflatable decelerator.

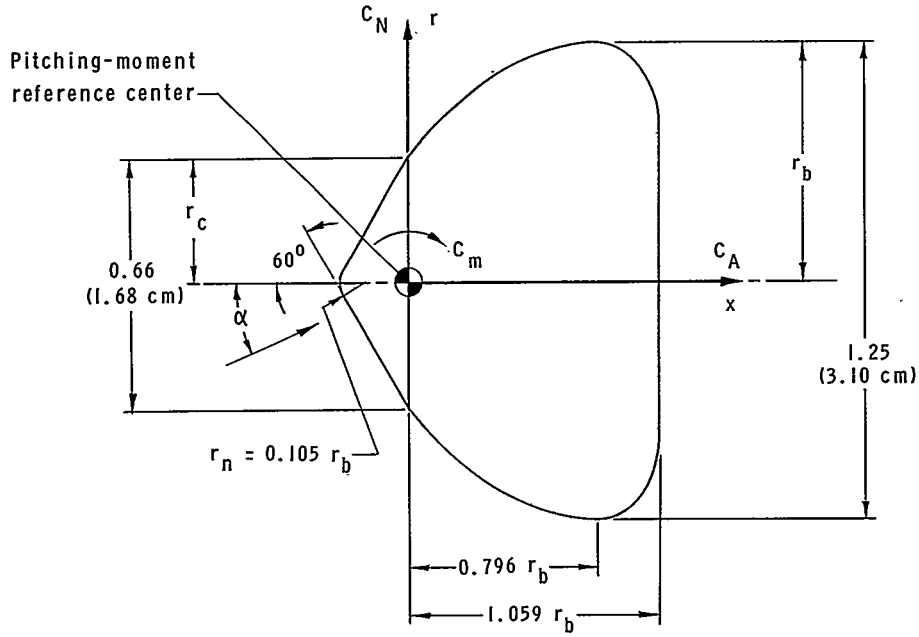

(a) Shape 1.

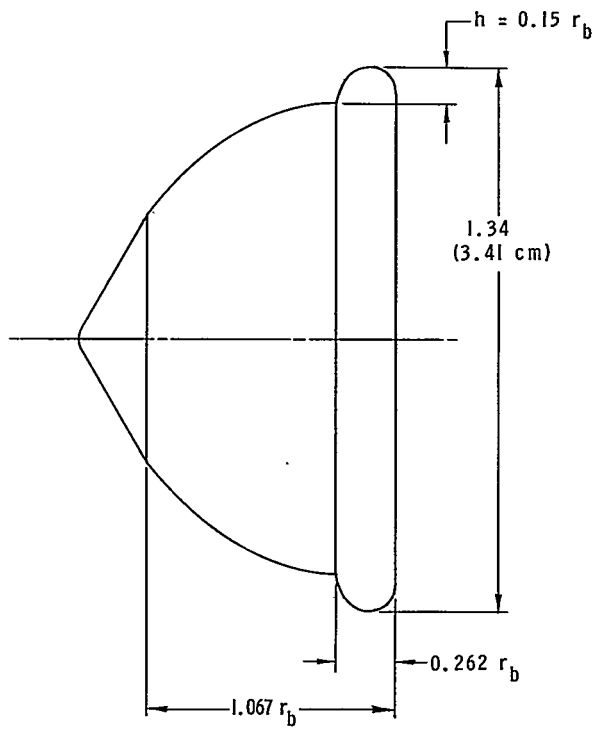

(b) Shape 1 with burble fence.

Figure 2.- Aerodynamic-forces models. Linear dimensions are in inches unless otherwise specified.

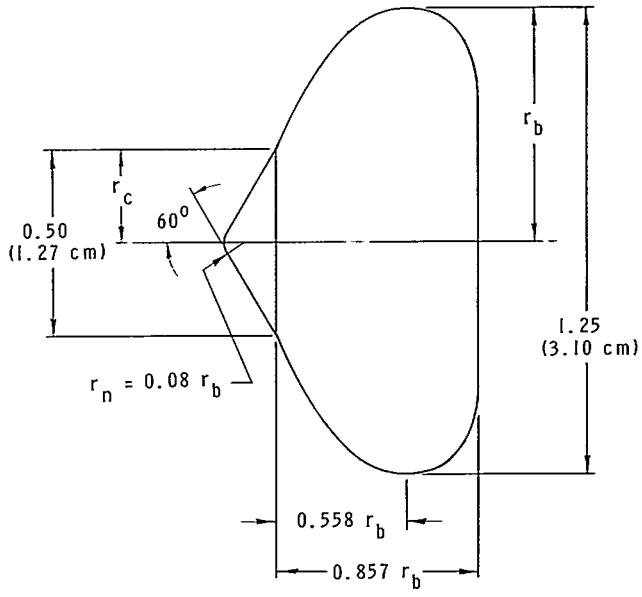

(c) Shape 2.

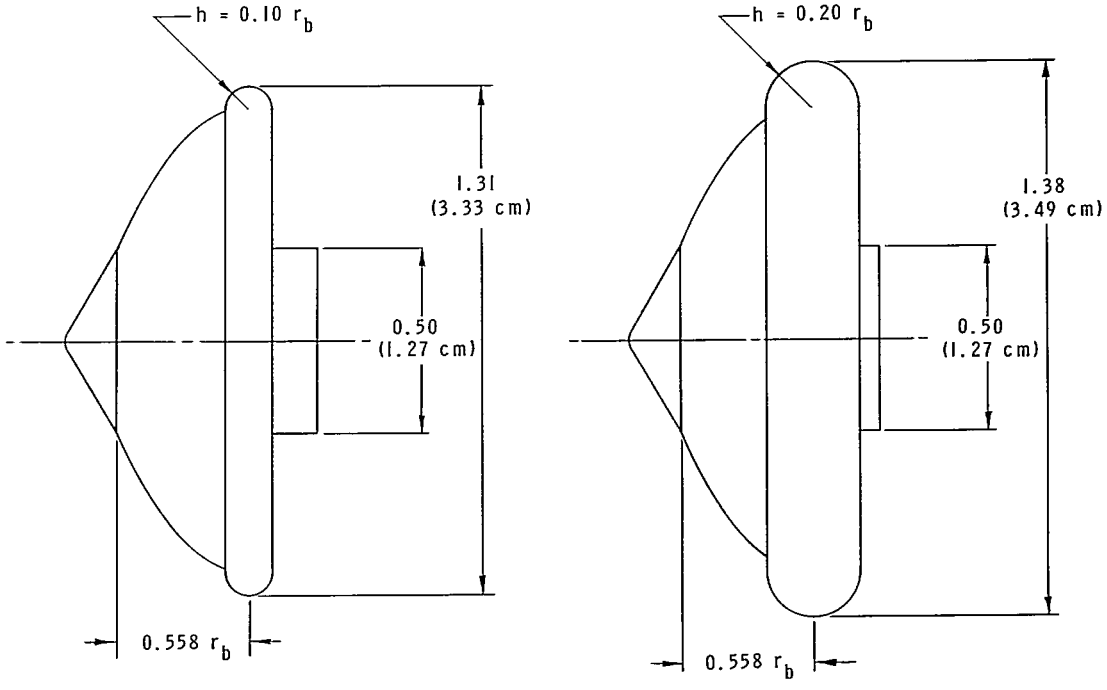

(d) Shape 2 with burble fences.

Figure 2.- Concluded.

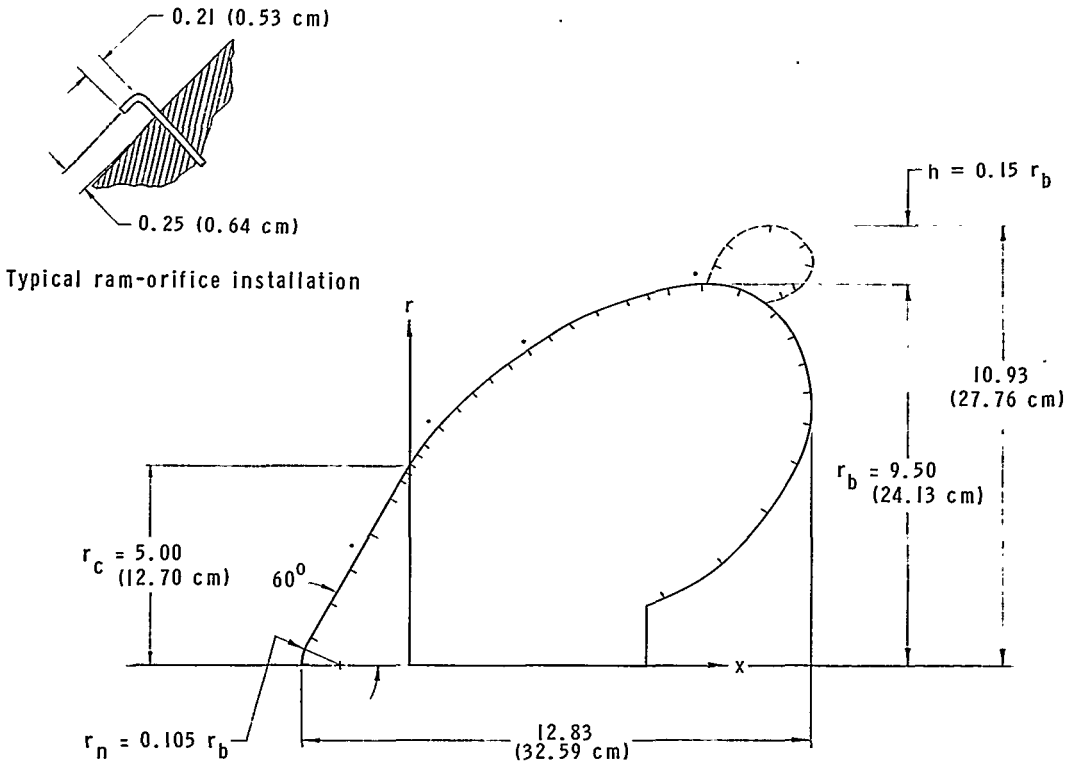

(a) Shape 1.

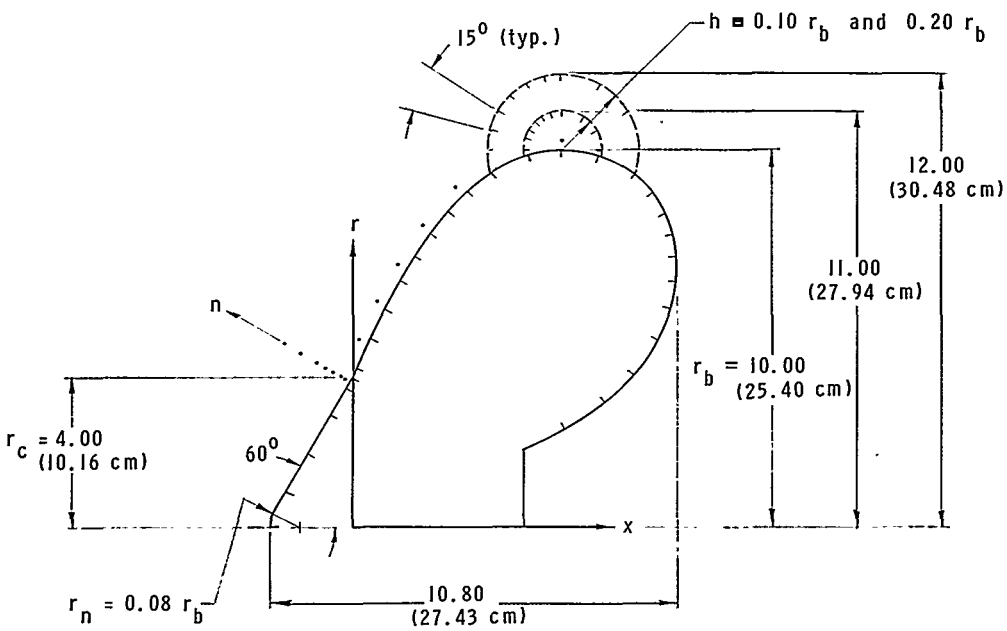

(b) Shape 2.

Figure 3.- Pressure-distribution models. Tick marks denote static-pressure orifices, and dots denote ram-pressure orifices. Linear dimensions are in inches unless otherwise specified.

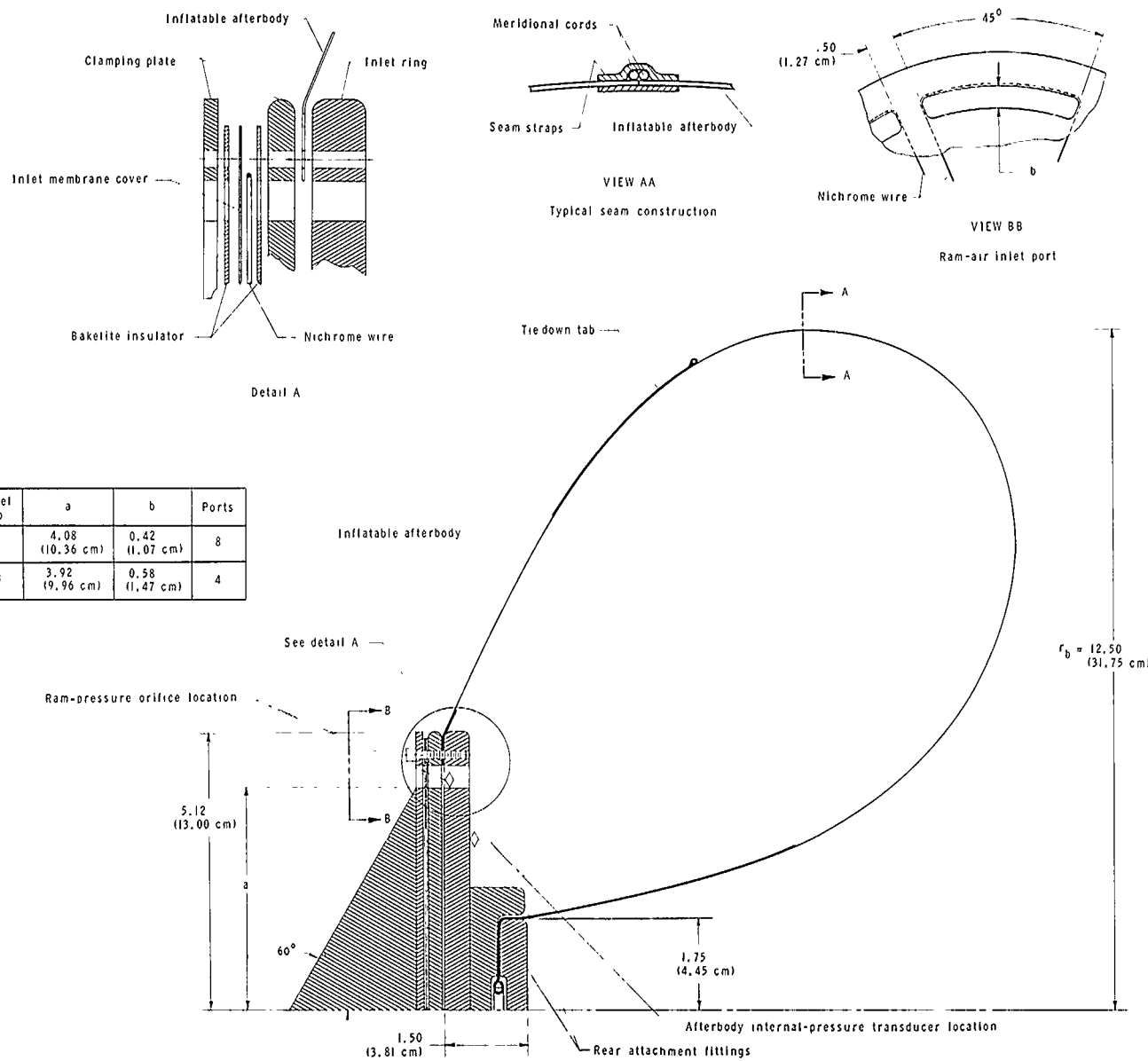

Model No	a	b	Ports
A	4.08 (10.36 cm)	0.42 (1.07 cm)	8
B	3.92 (9.96 cm)	0.58 (1.47 cm)	4

Figure 4.- Details of ram-inflation model with membrane-covered inlets. Linear dimensions are in inches unless otherwise specified.

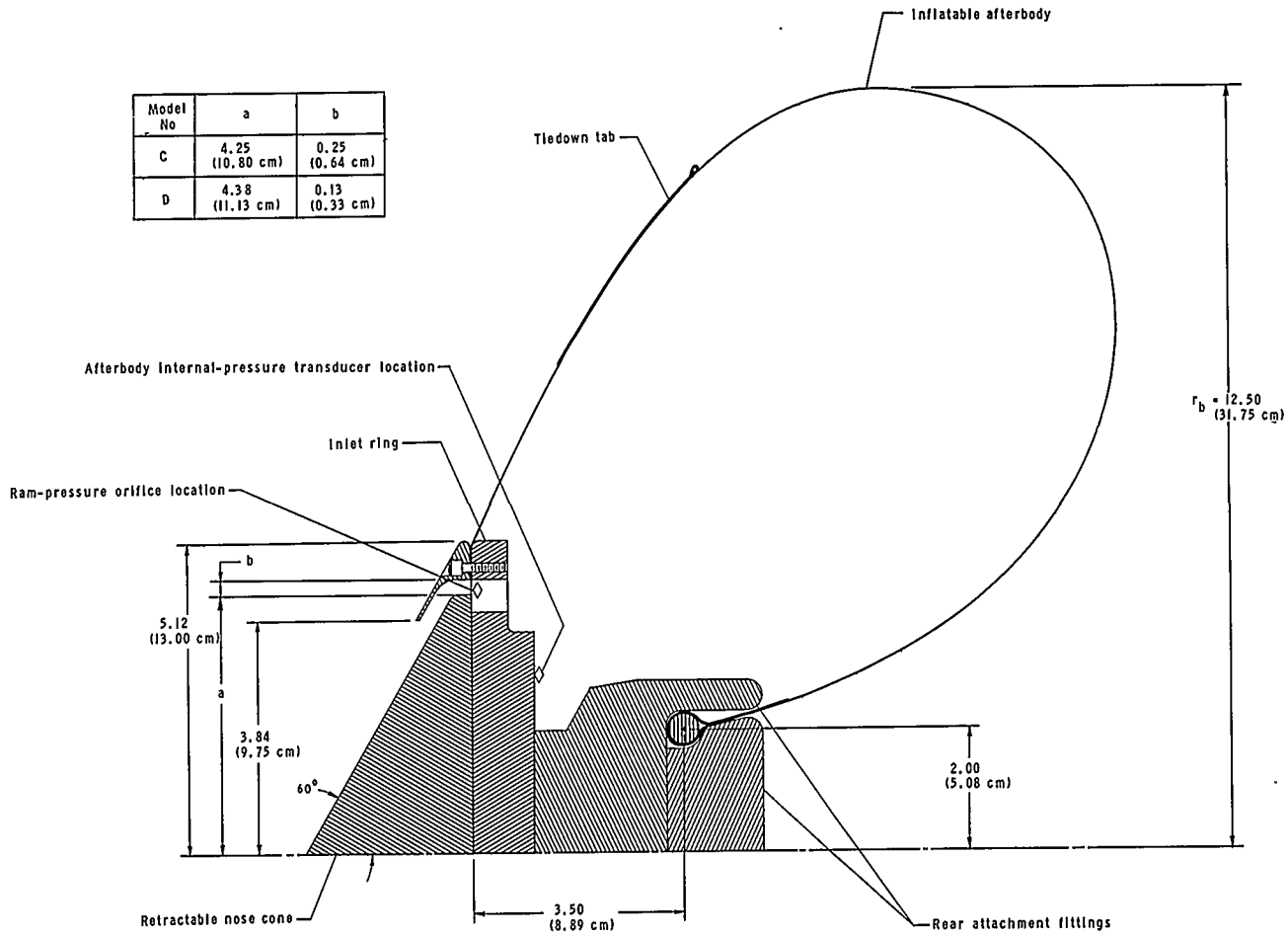

Model No	a	b
C	4.25 (10.80 cm)	0.25 (0.64 cm)
D	4.38 (11.13 cm)	0.13 (0.33 cm)

Figure 5.- Details of ram-inflation model with retractable nose-cone inlet. Cone is shown in retracted position. Linear dimensions are in inches unless otherwise specified.

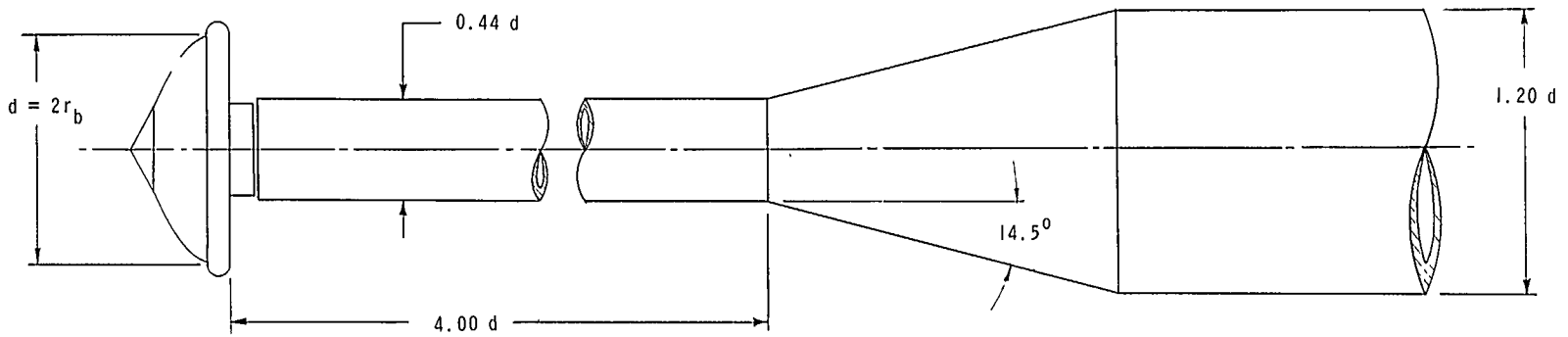

Figure 6.- Aerodynamic-forces model-sting configuration.

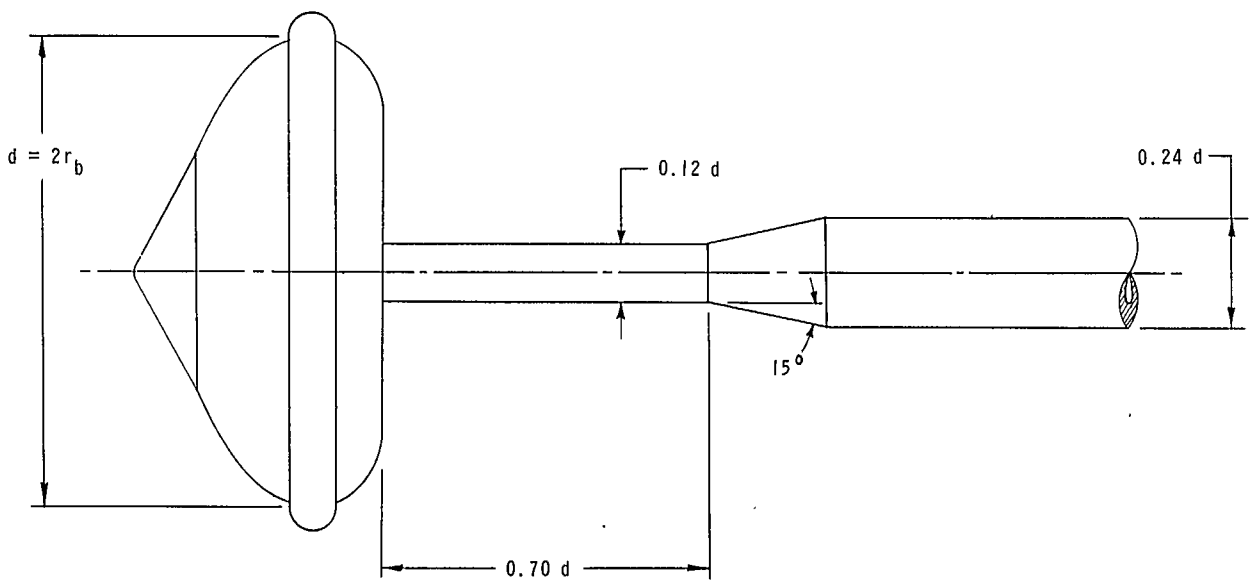

Figure 7.- Pressure-distribution model-sting configuration.

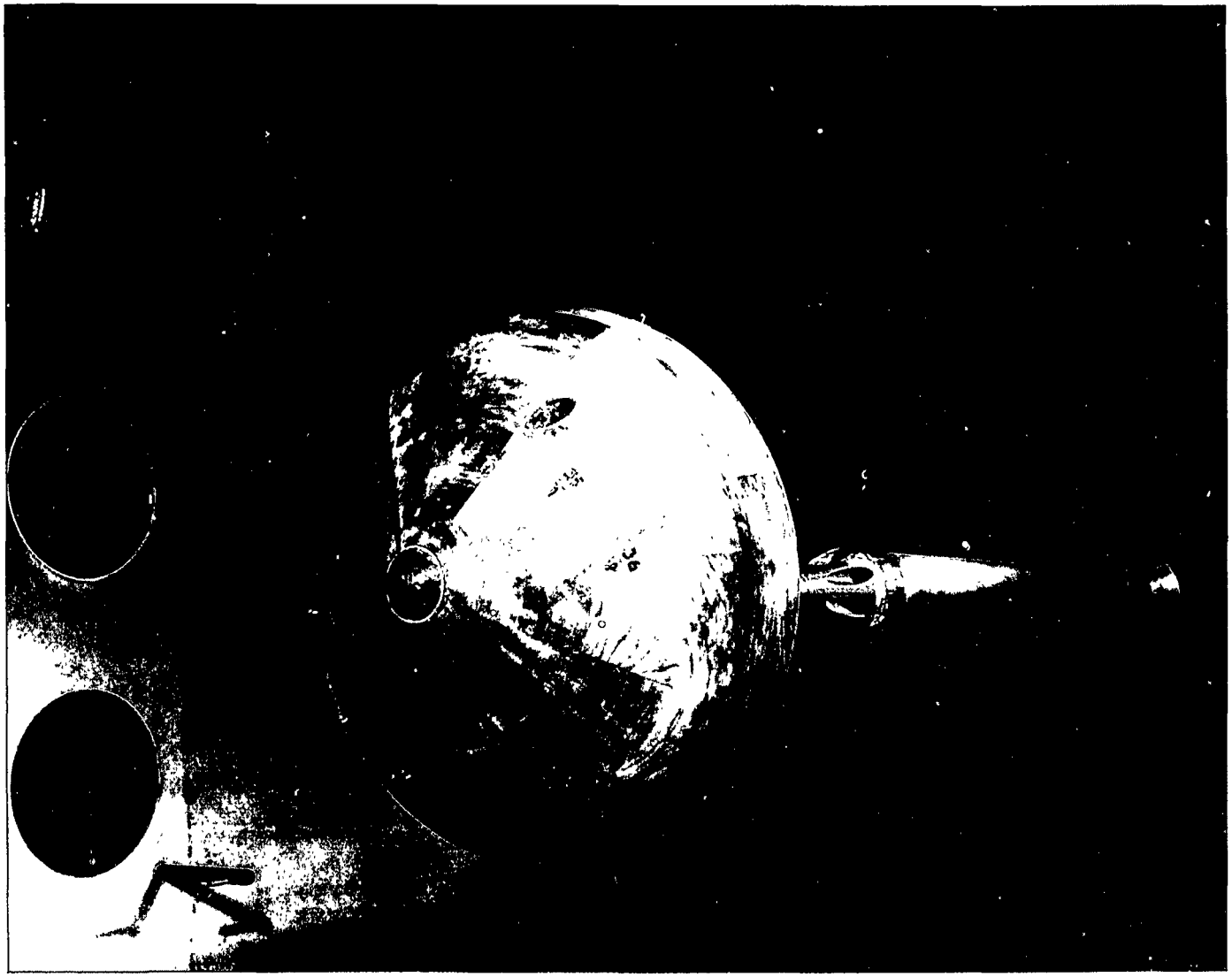

L-68-7288

Figure 8.- Front view of typical pressure-distribution model test setup in the Langley 9- by 6-foot thermal structures tunnel.

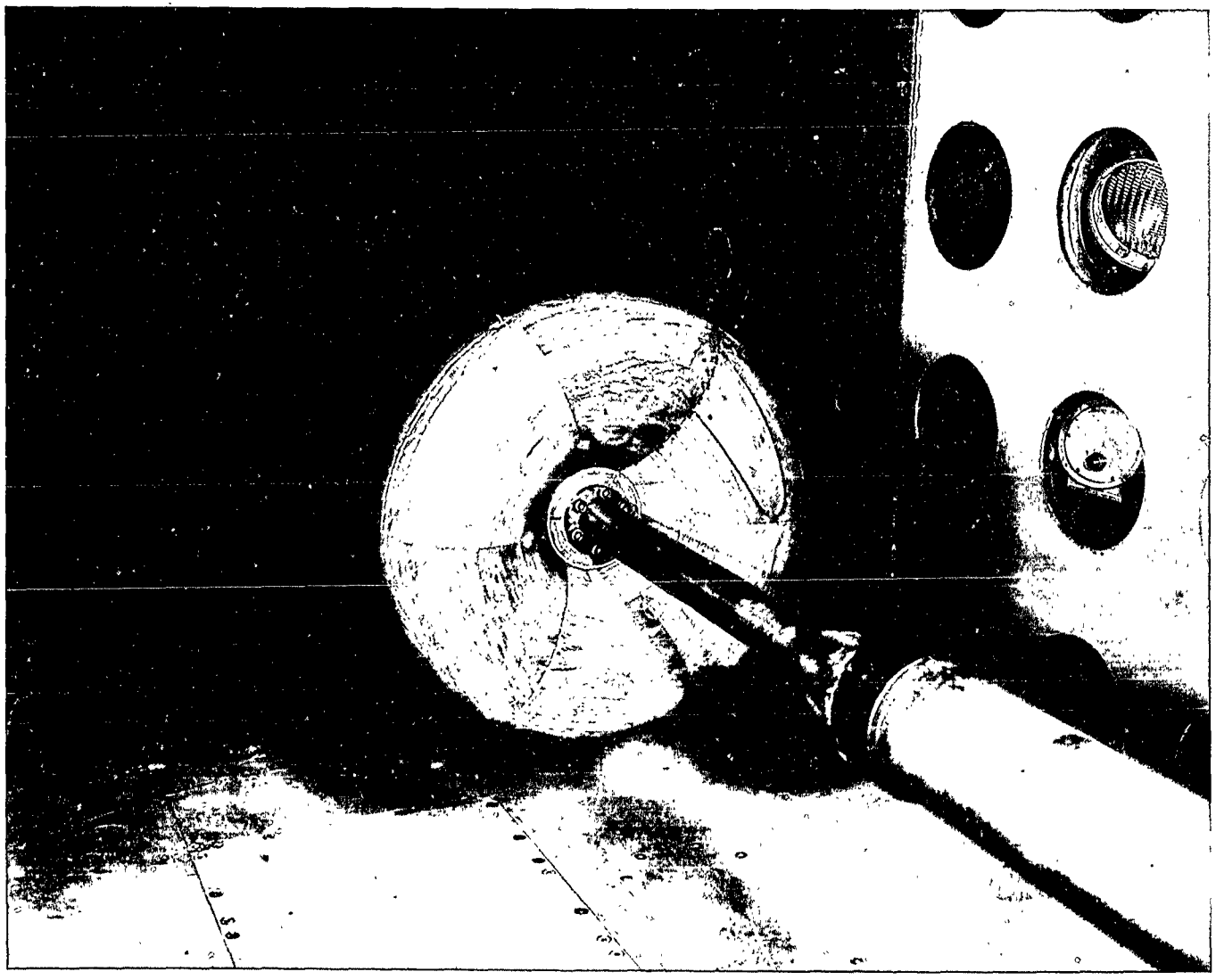

L-68-7290

Figure 9.- Rear view of typical pressure-distribution model test setup in the Langley 9- by 6-foot thermal structures tunnel.

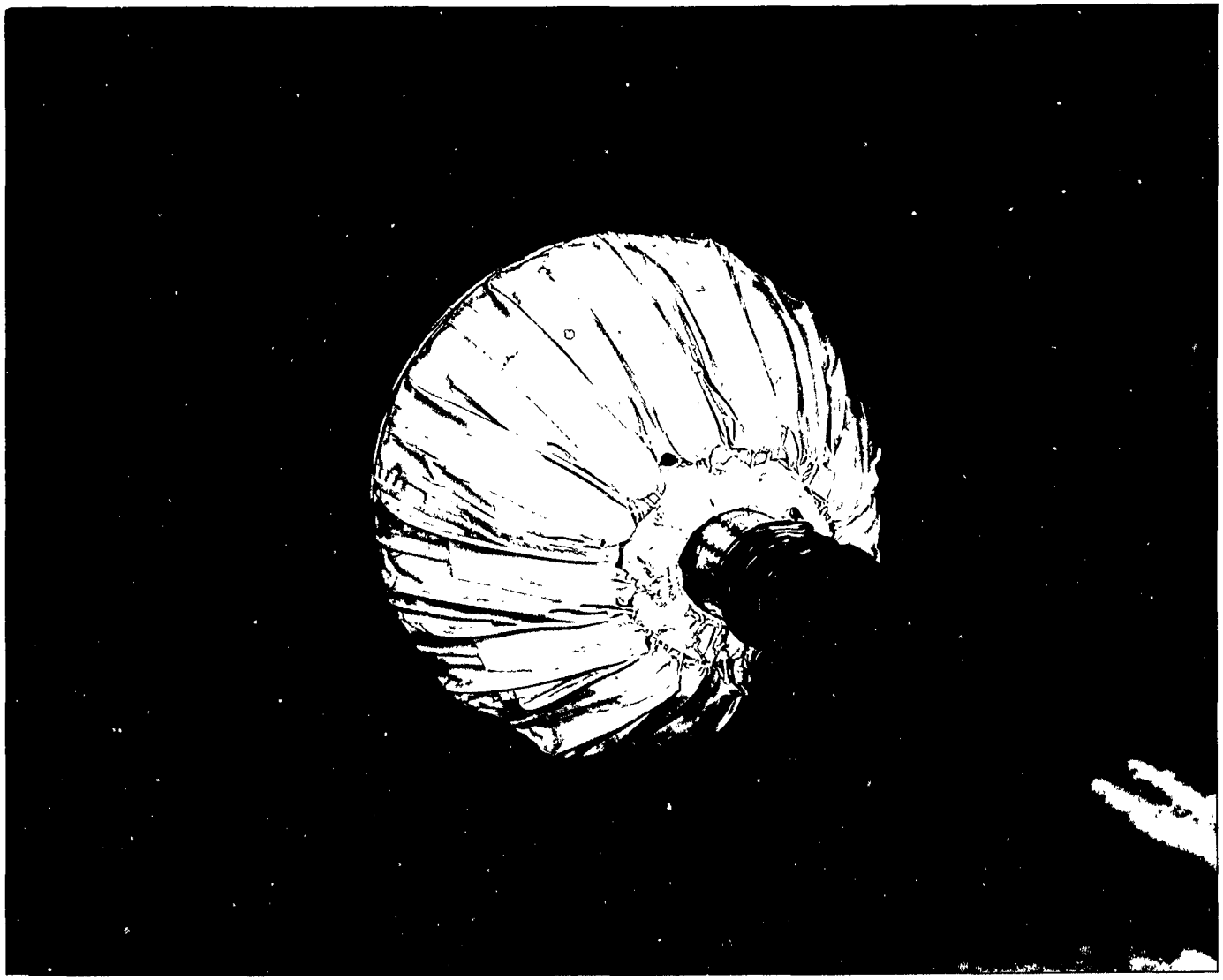

L-68-8320

Figure 10.- Rear view of a ram-inflation model of an attached inflatable decelerator in the Langley 9- by 6-foot thermal structures tunnel.

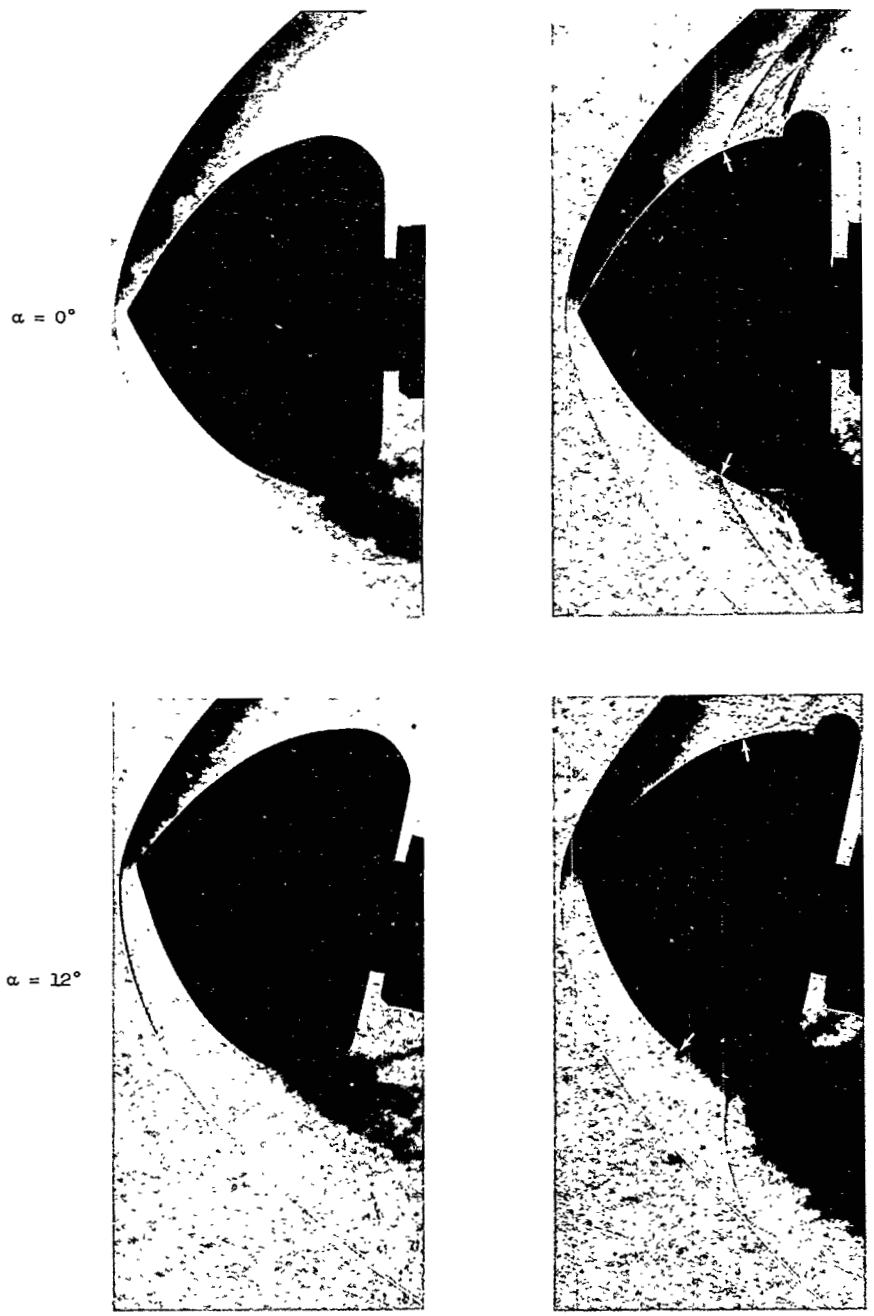

(a) $R \approx 1.1 \times 10^6$.

L-70-1554

Figure 11.- Schlieren photographs of shape 1 aerodynamic-forces model at Mach 3.0. Arrowheads indicate location of boundary-layer separation point.

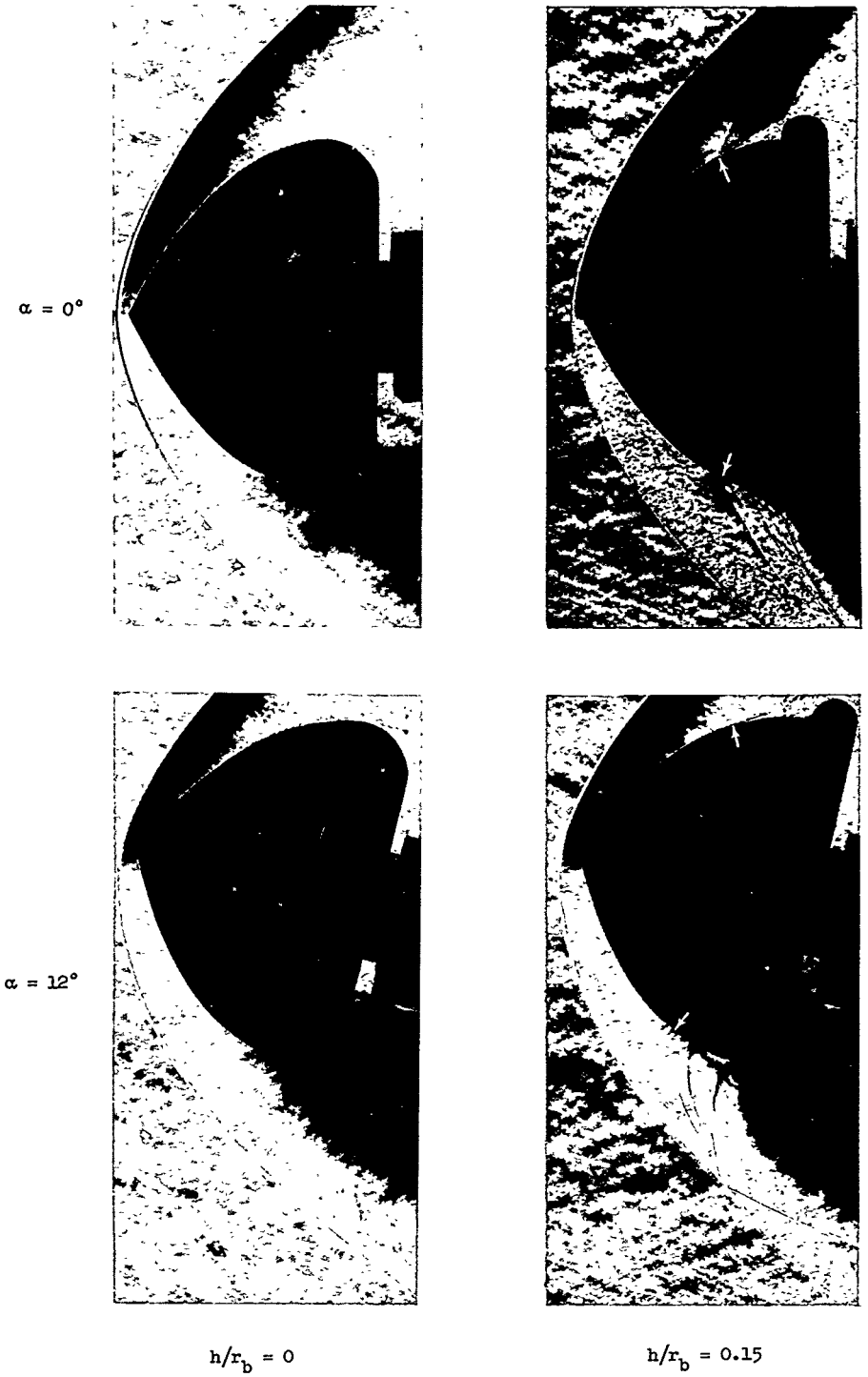

(b) $R \approx 3.0 \times 10^6$.

L-70-1555

Figure 11.- Concluded.

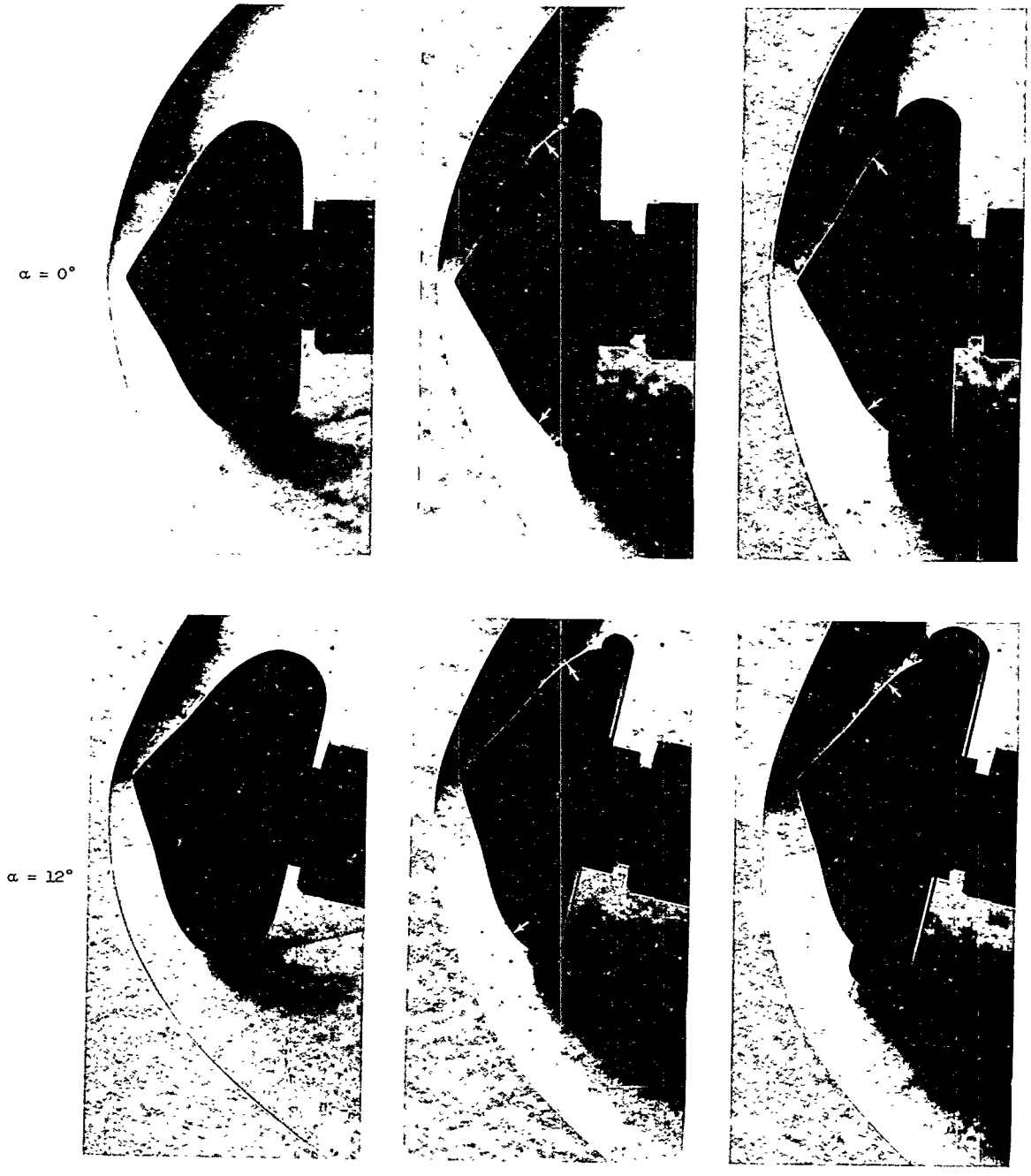

(a) $R \approx 1.1 \times 10^6$.

L-70-1556

Figure 12.- Schlieren photographs of shape 2 aerodynamic-forces model at Mach 3.0. Arrowheads indicate location of boundary-layer separation point.

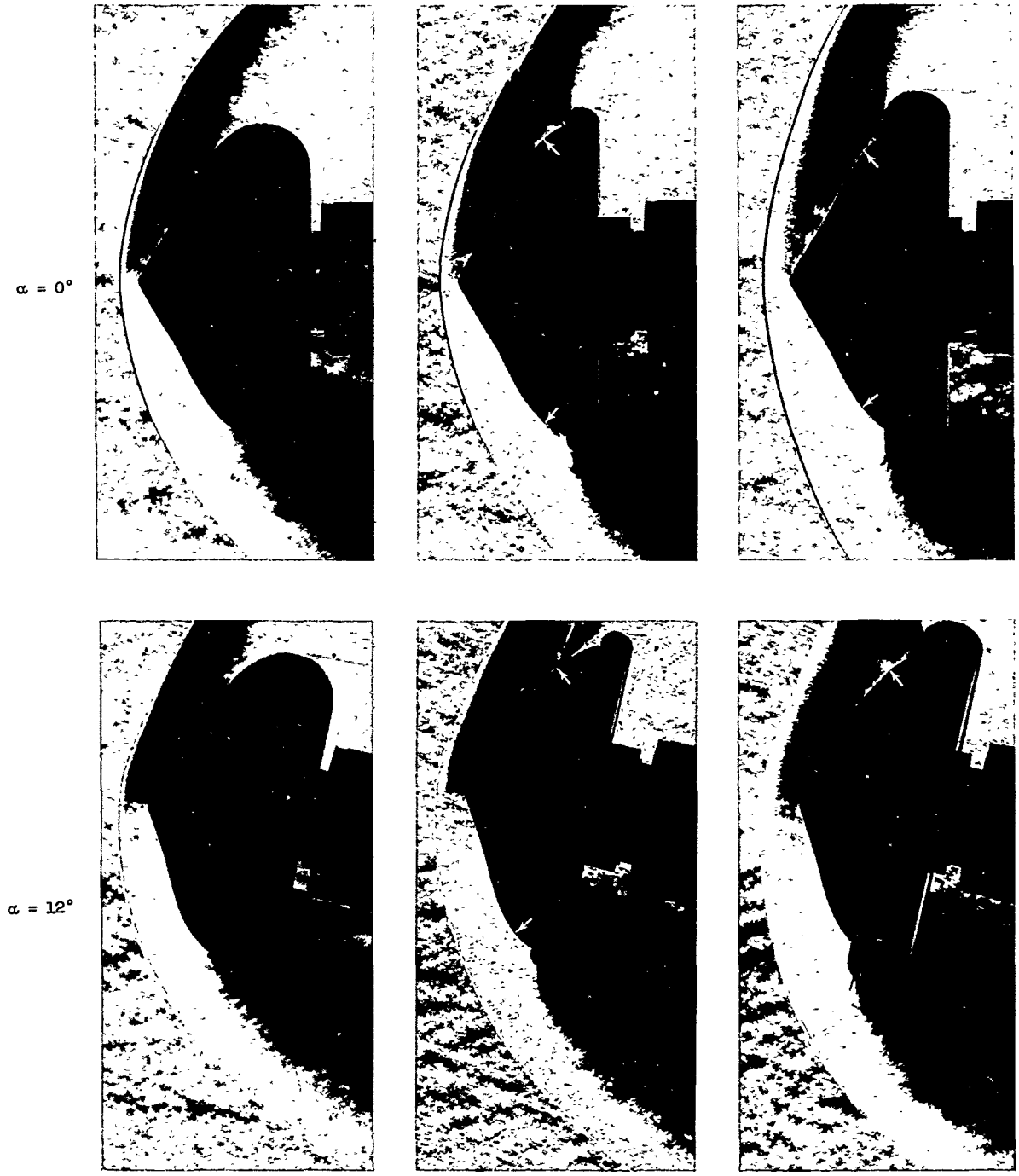

(b) $R \approx 3.0 \times 10^6$.

L-70-1557

Figure 12.- Concluded.

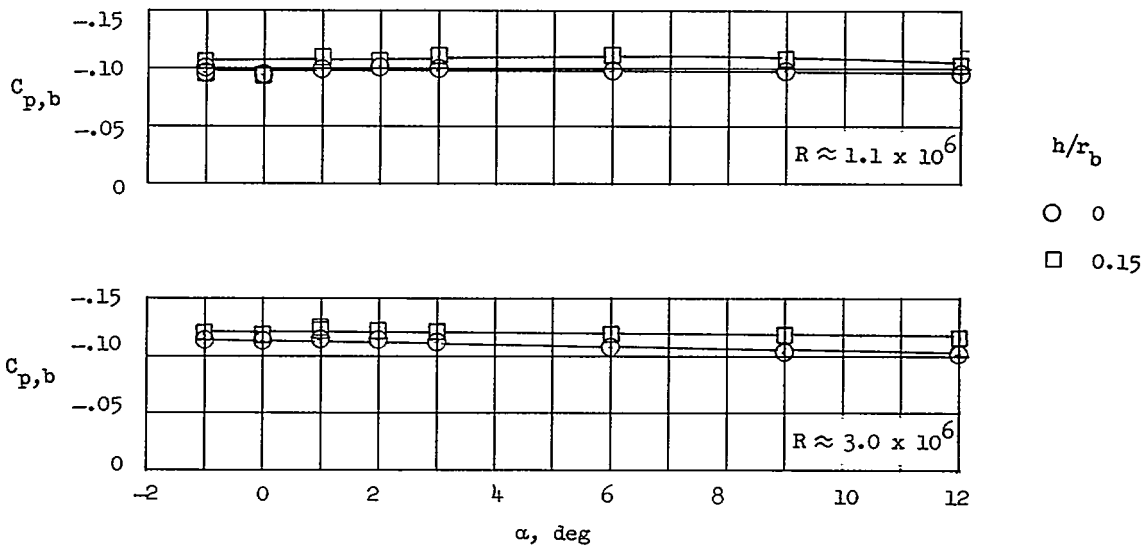

(a) Shape 1.

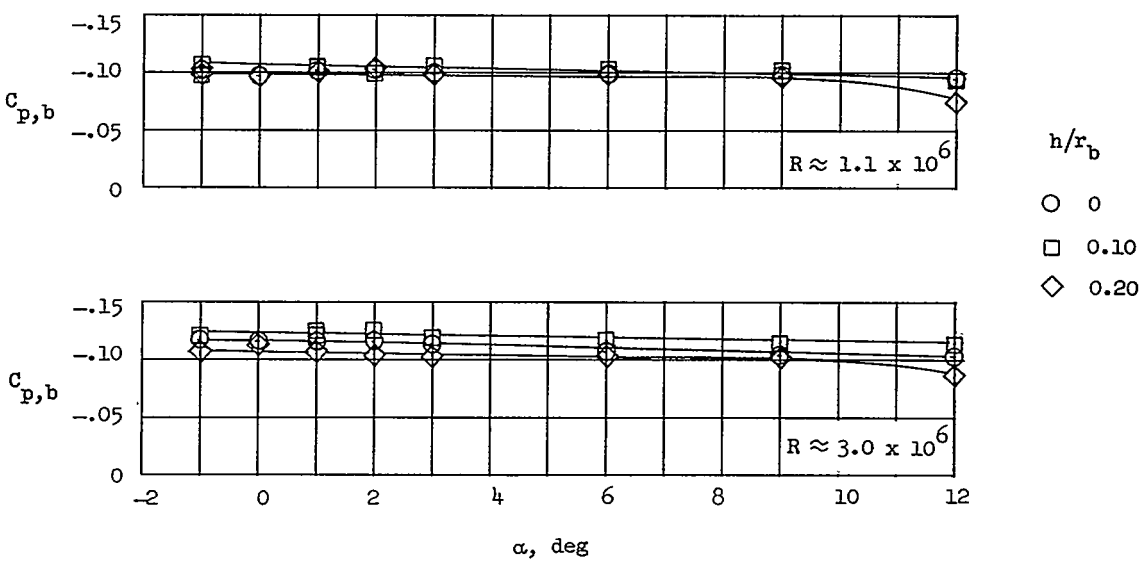

(b) Shape 2.

Figure 13.- Variation of model base-pressure coefficient with angle of attack.

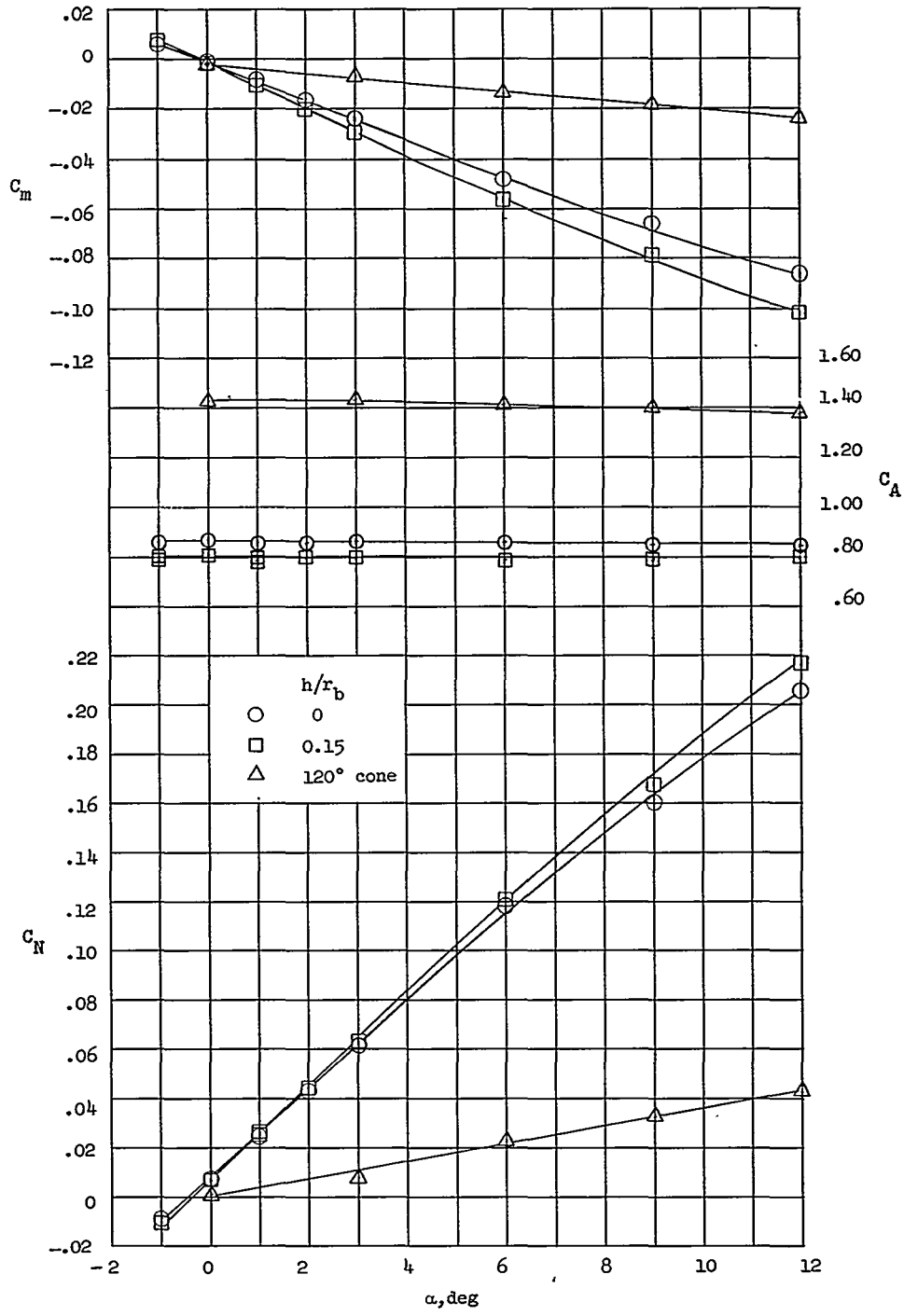

(a) $R \approx 1.1 \times 10^6$.

Figure 14.- Longitudinal aerodynamic characteristics of attached-inflatable-decelerator shape 1 at Mach 3.0. Axial-force coefficients are corrected to free-stream static pressure at the model base.

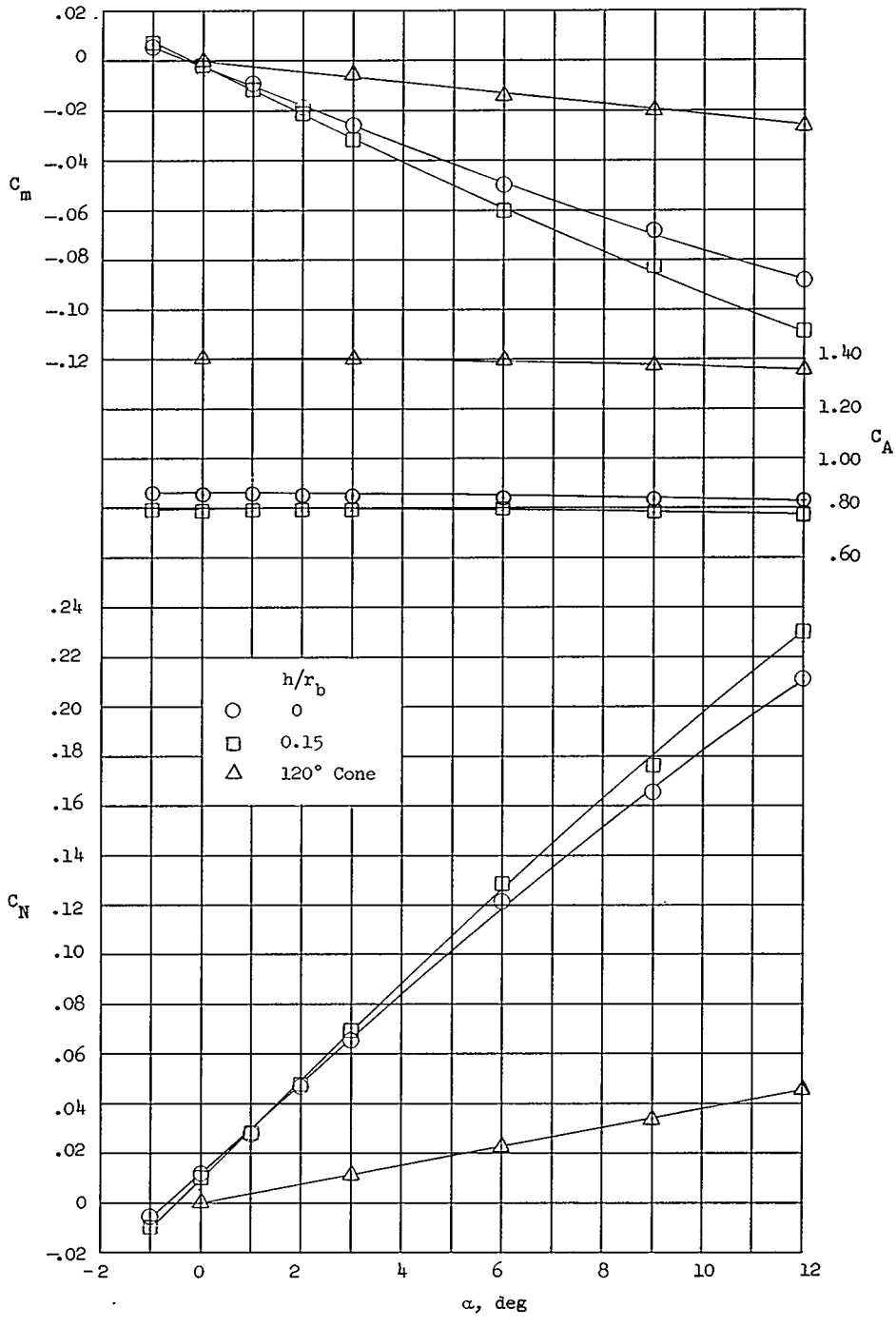

(b) $R \approx 3.0 \times 10^6$.

Figure 14.- Concluded.

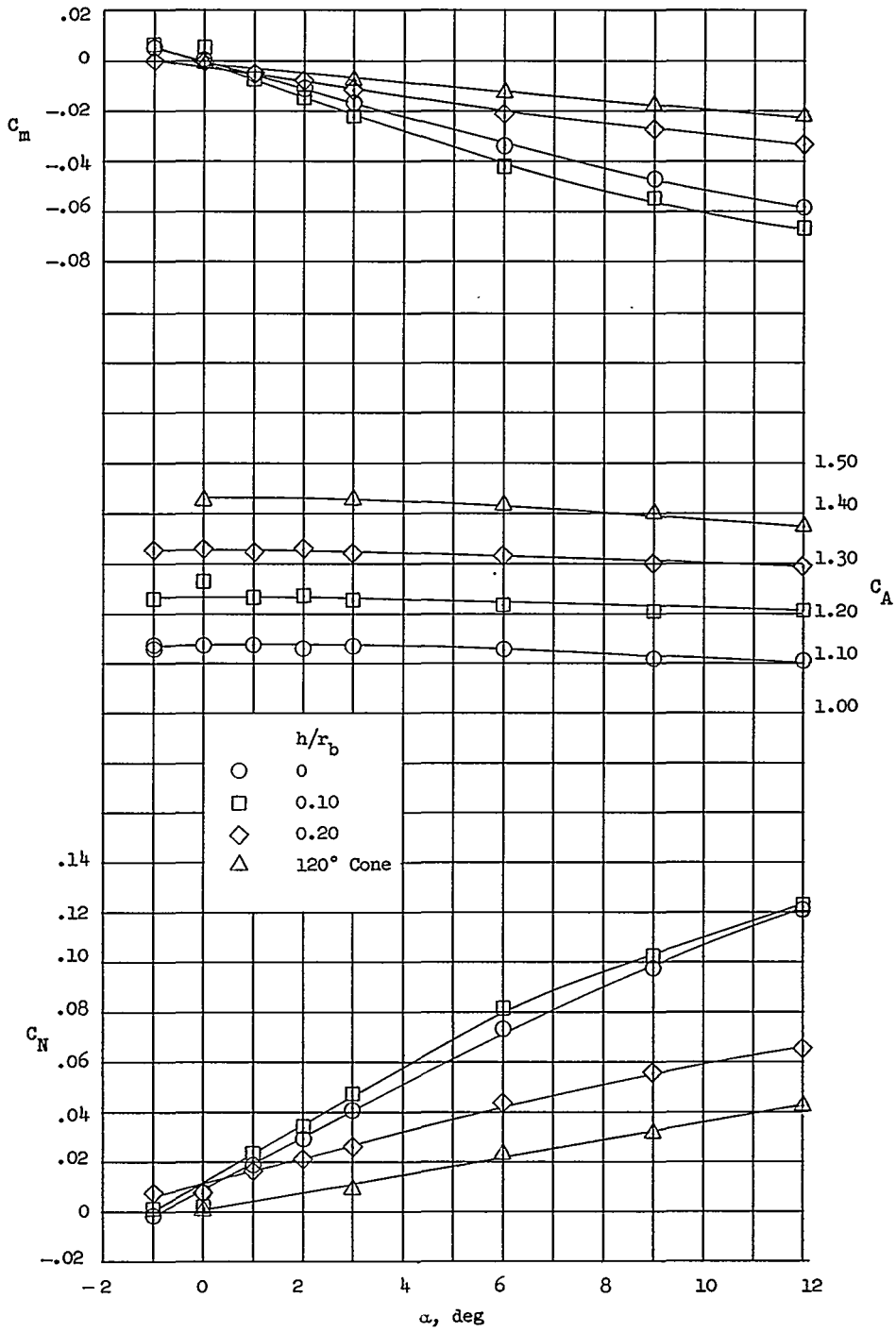

(a) $R \approx 1.1 \times 10^6$.

Figure 15.- Longitudinal aerodynamic characteristics of attached-inflatable-decelerator shape 2 at Mach 3.0. Axial-force coefficients are corrected to free-stream static pressure at the model base.

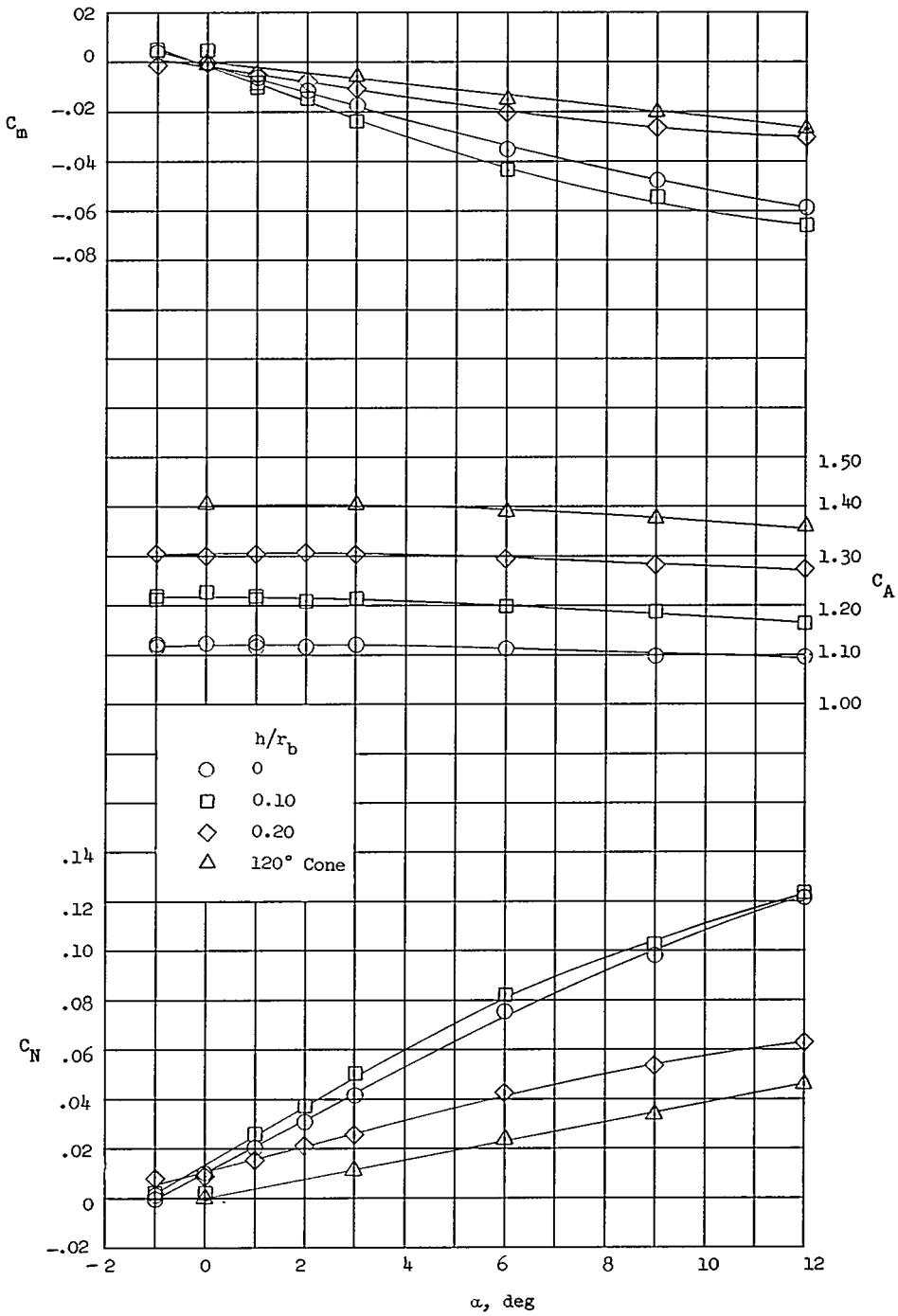

(b) $R \approx 3.0 \times 10^6$.

Figure 15.- Concluded.

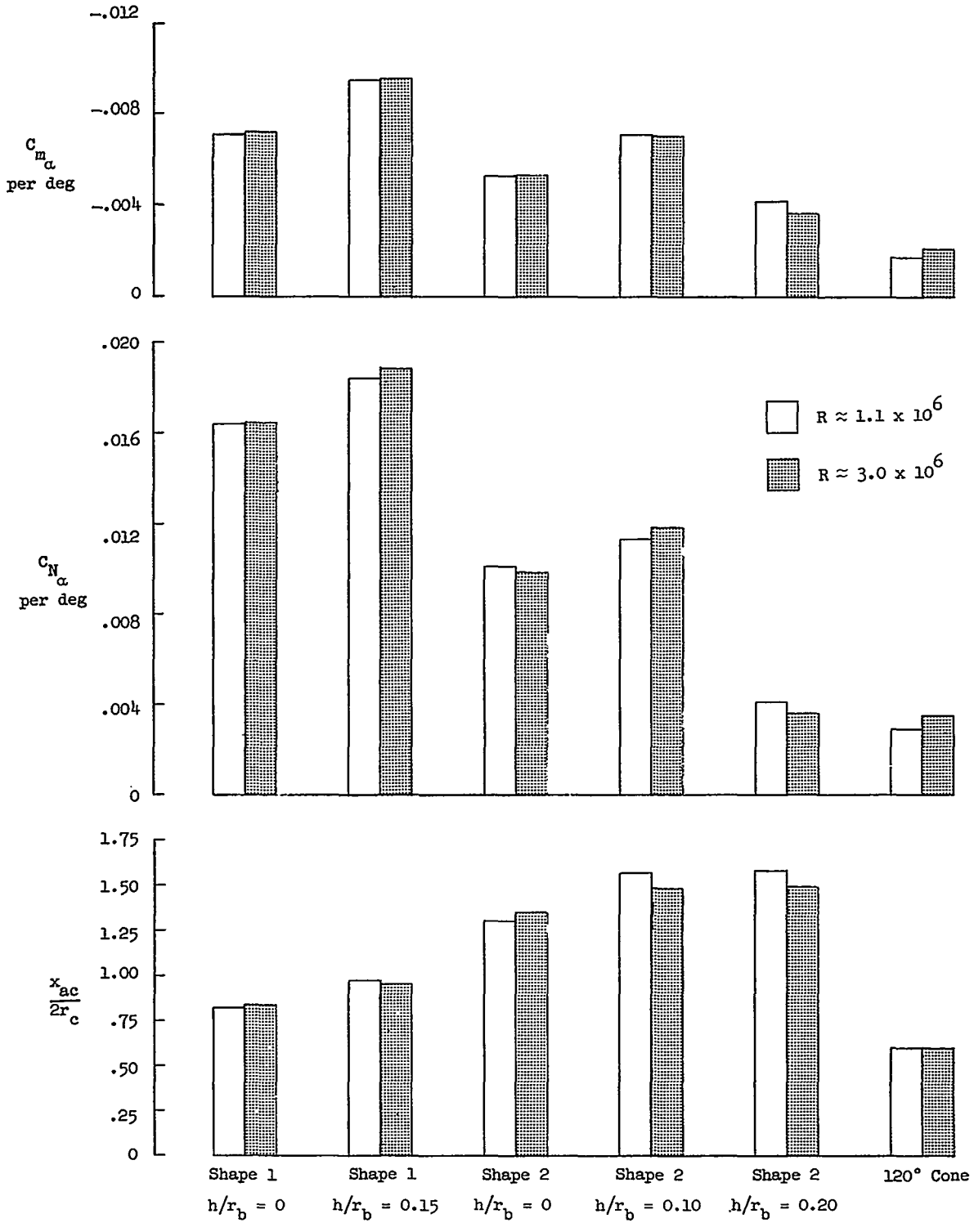

Figure 16.- C_{m_α}, C_{N_α}, and $x_{ac}/2r_c$ for attached-inflatable-decelerator shapes 1 and 2 and a reference 120° cone.

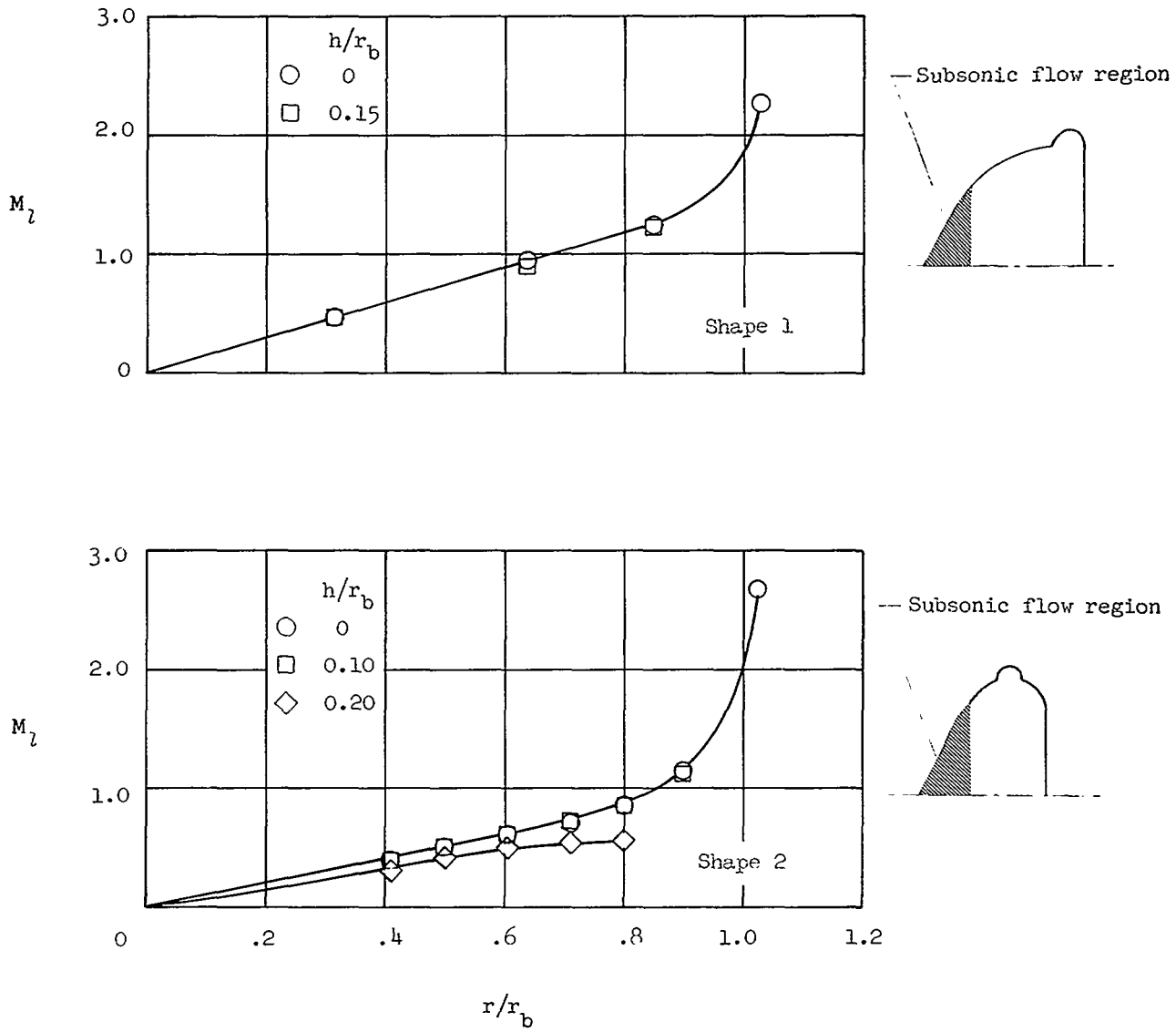

Figure 17.- Surface Mach number distributions obtained from static and total pressures (total pressures measured 0.25 inch (0.63 cm) above surface).

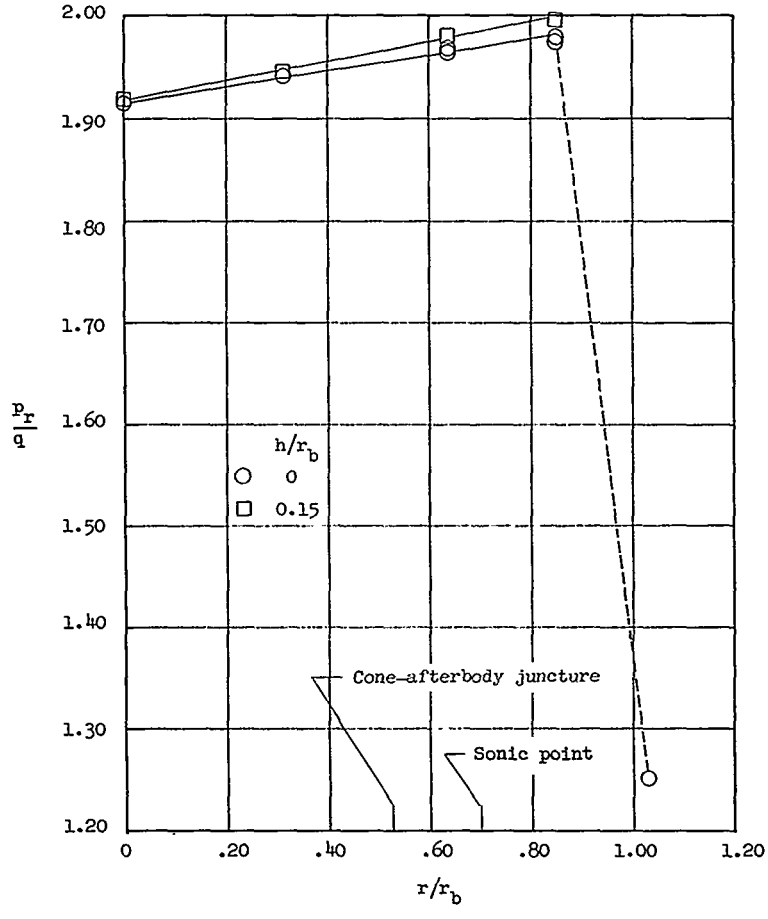

(a) Shape 1, along surface (p_r measured 0.25 inch (0.63 cm) above surface).

Figure 18.- Ram pressures.

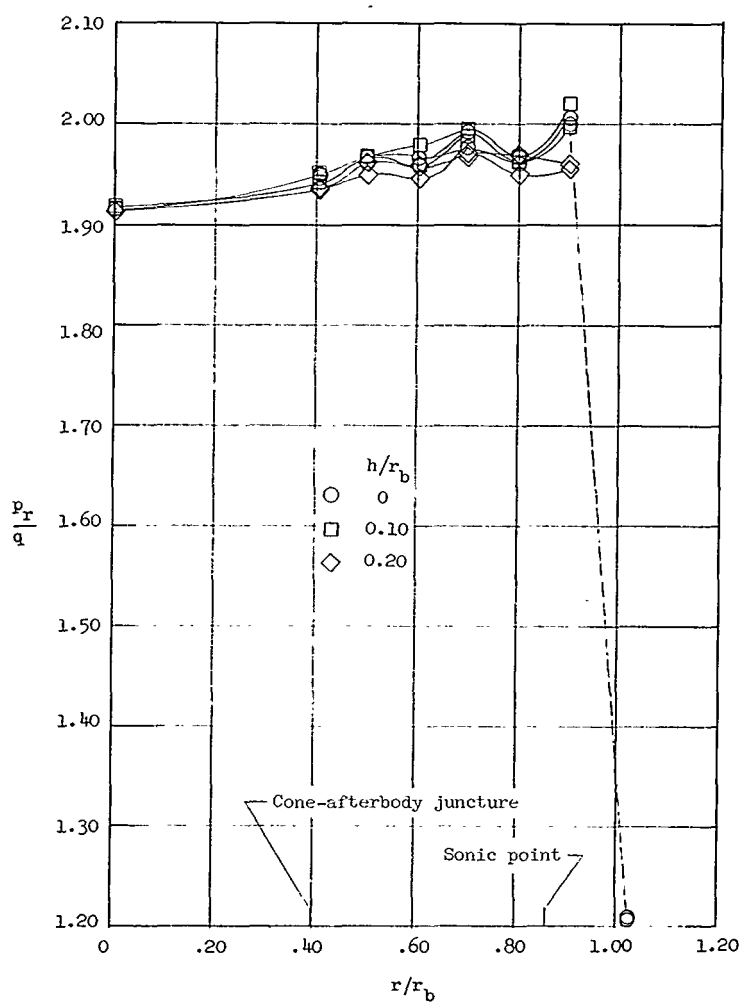

(b) Shape 2, along surface (p_r measured 0.25 inch (0.63 cm) above surface).

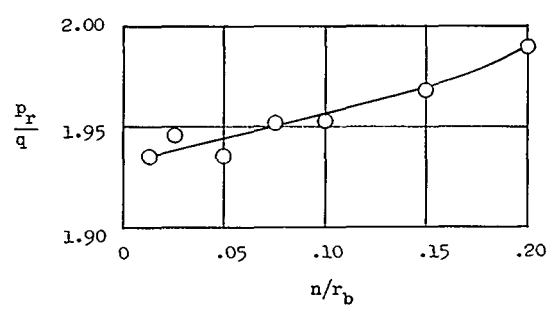

(c) Shape 2, normal to surface at $r/r_b \approx 0.40$.

Figure 18.- Concluded.

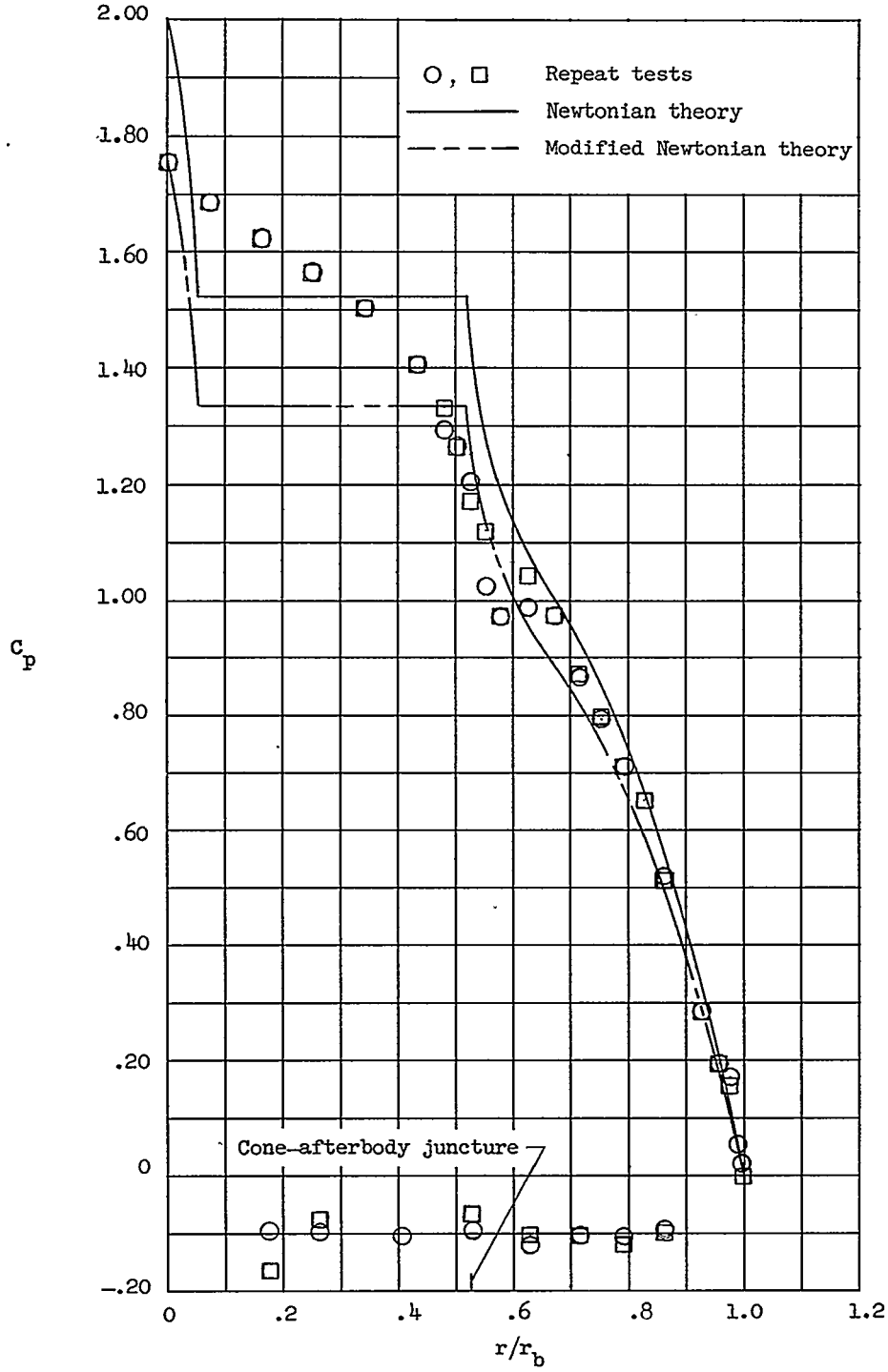

(a) $h/r_b = 0$.

Figure 19.- Experimental and theoretical pressures for shape 1.

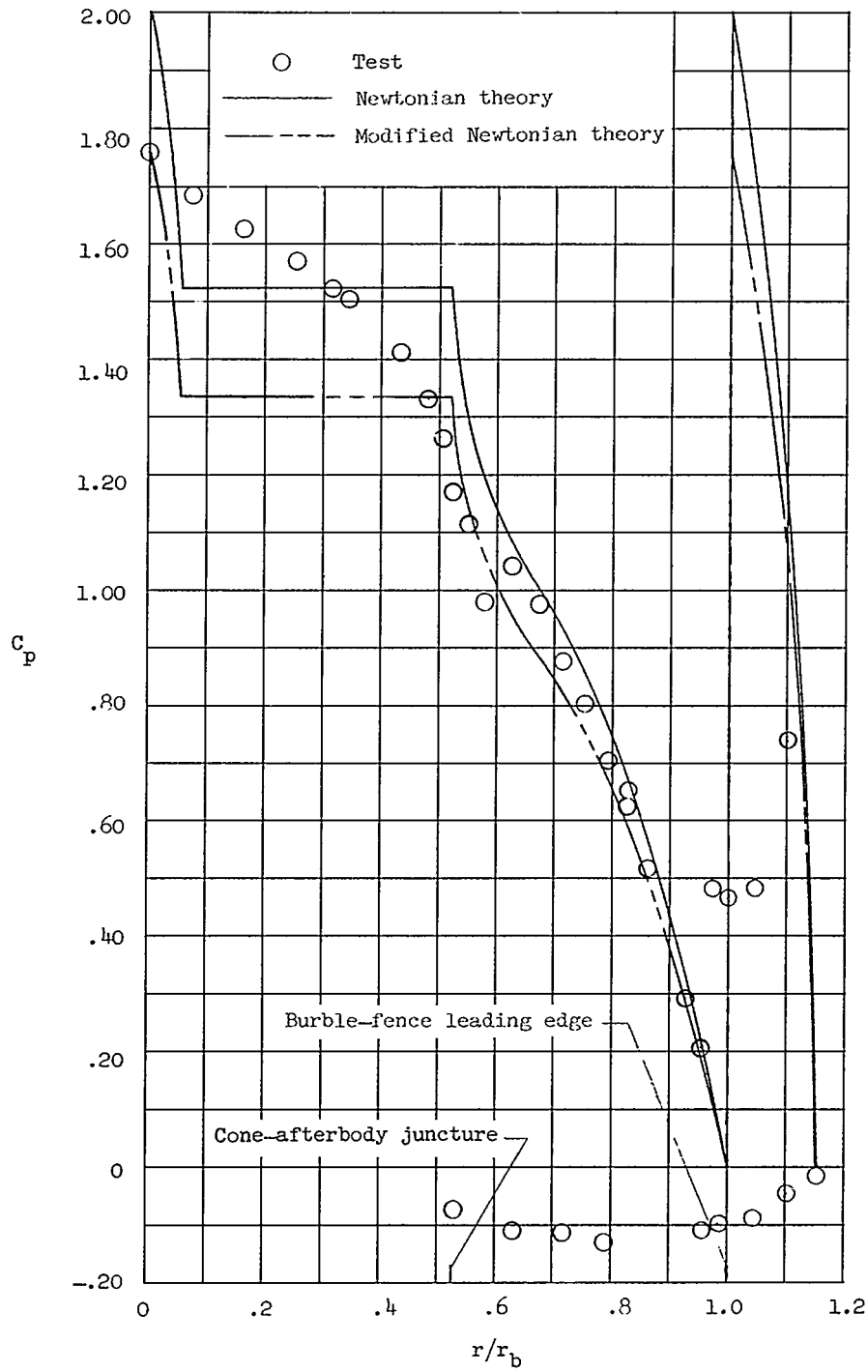

(b) $h/r_b = 0.15$.

Figure 19.- Concluded.

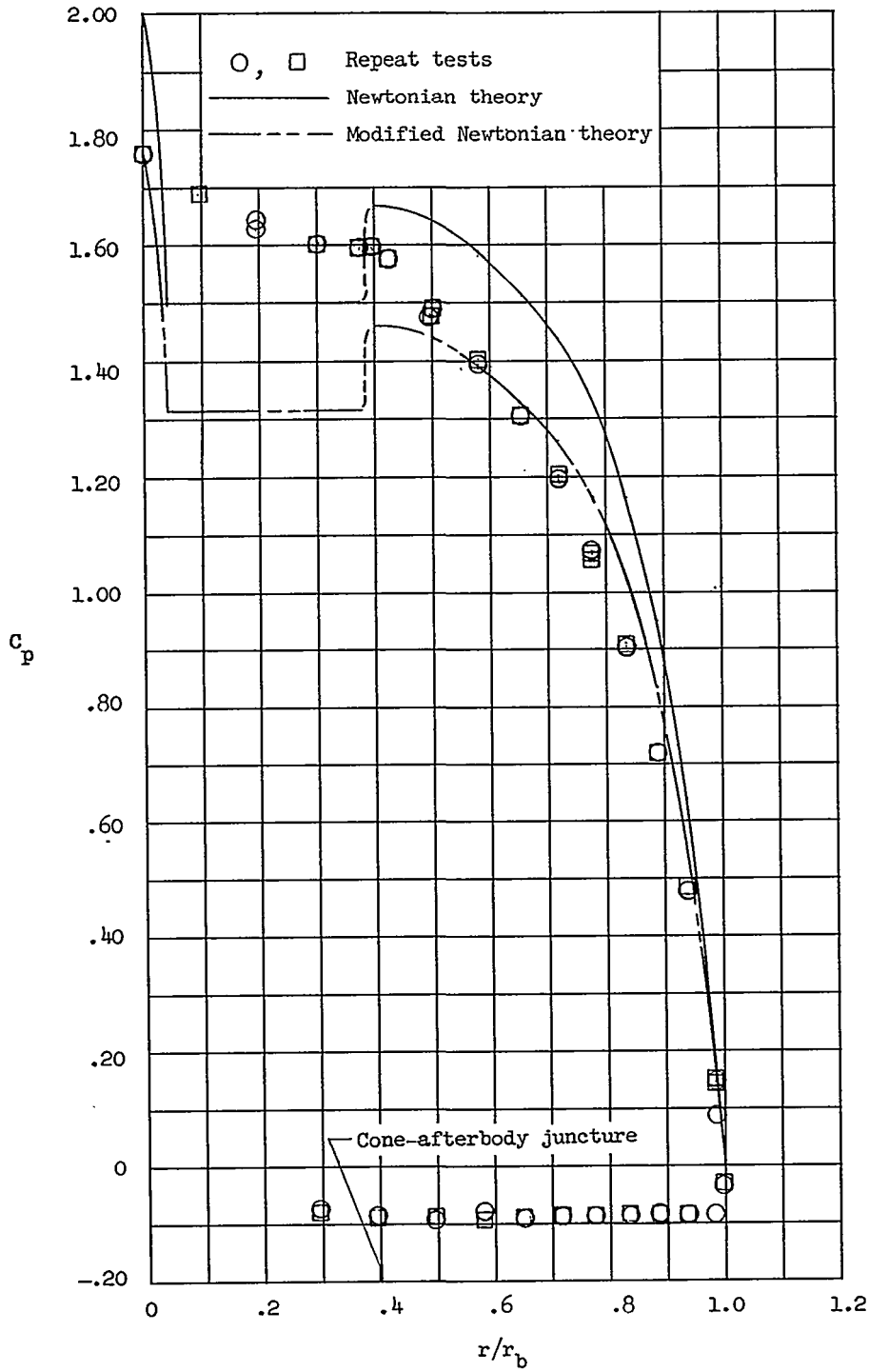

(a) $h/r_b = 0$.

Figure 20.- Experimental and theoretical pressures for shape 2.

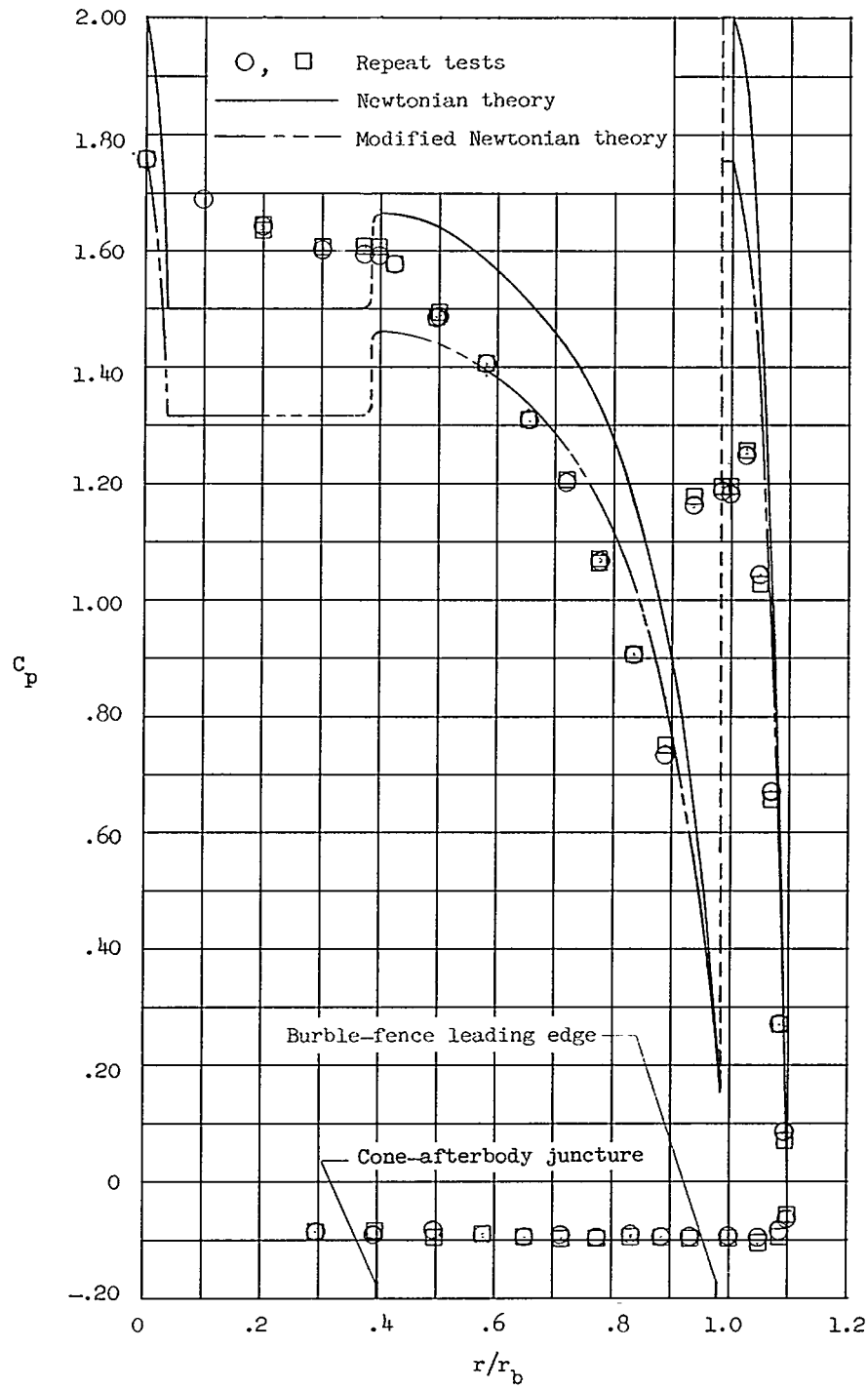

(b) $h/r_b = 0.10$.

Figure 20.- Continued.

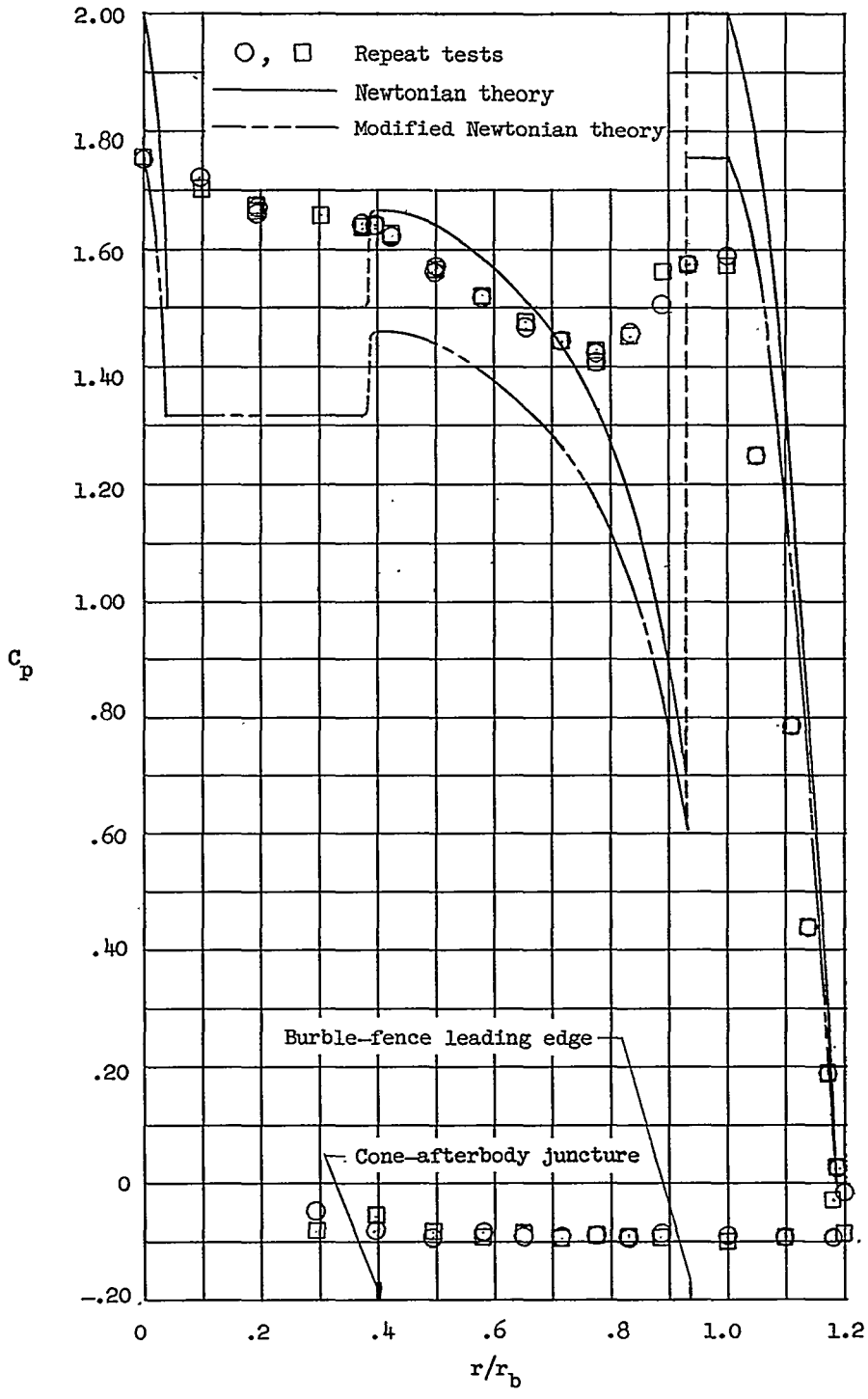

(c) $h/r_b = 0.20$.

Figure 20.- Concluded.

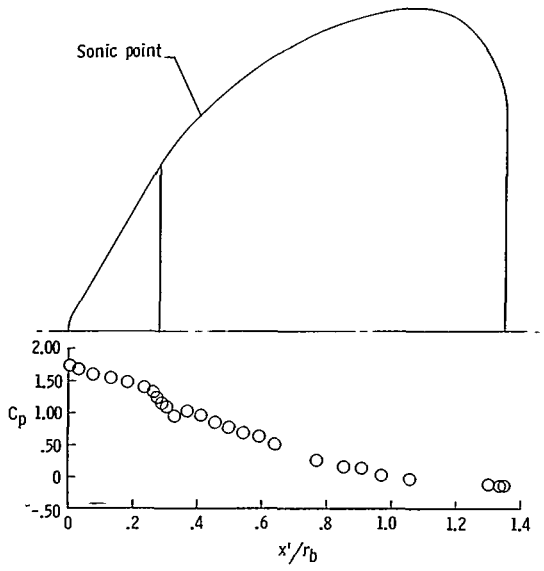

(a) Shape 1, $h/r_b = 0$.

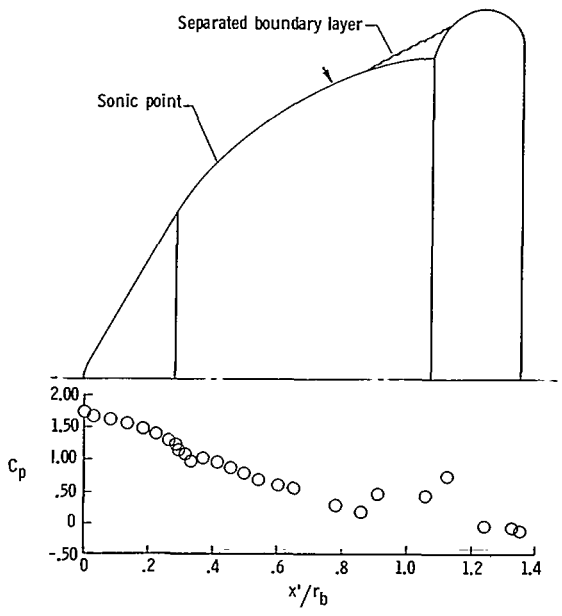

(b) Shape 1, $h/r_b = 0.15$.

Figure 21.- Illustrations of burble-fence effects on the boundary layer and on pressure distribution. Sketches of the separated boundary layer were determined from the pressure distributions shown. Arrowheads indicate the location of the boundary-layer separation point determined from schlieren photographs.

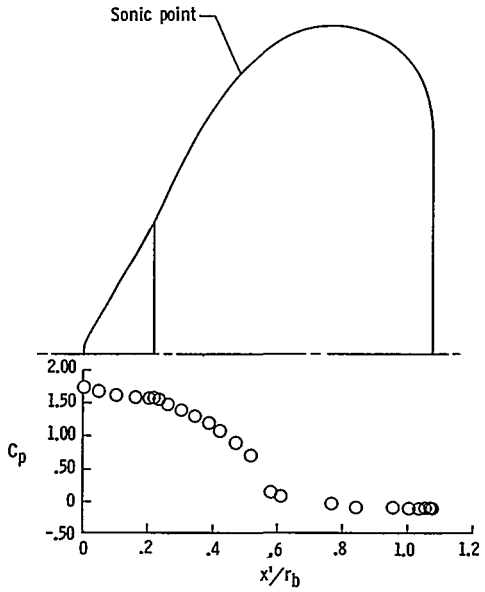

(c) Shape 2, $h/r_b = 0$.

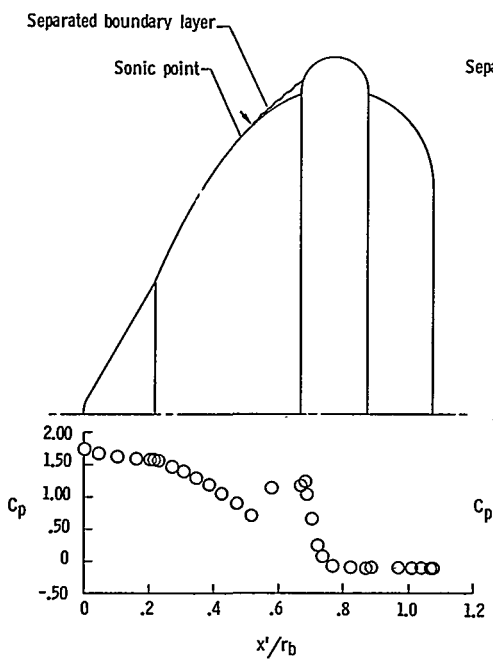

(d) Shape 2, $h/r_b = 0.10$.

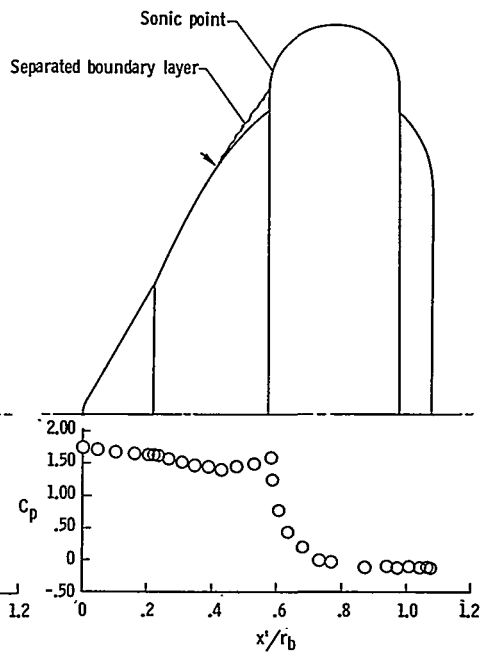

(e) Shape 2, $h/r_b = 0.20$.

Figure 21.- Concluded.

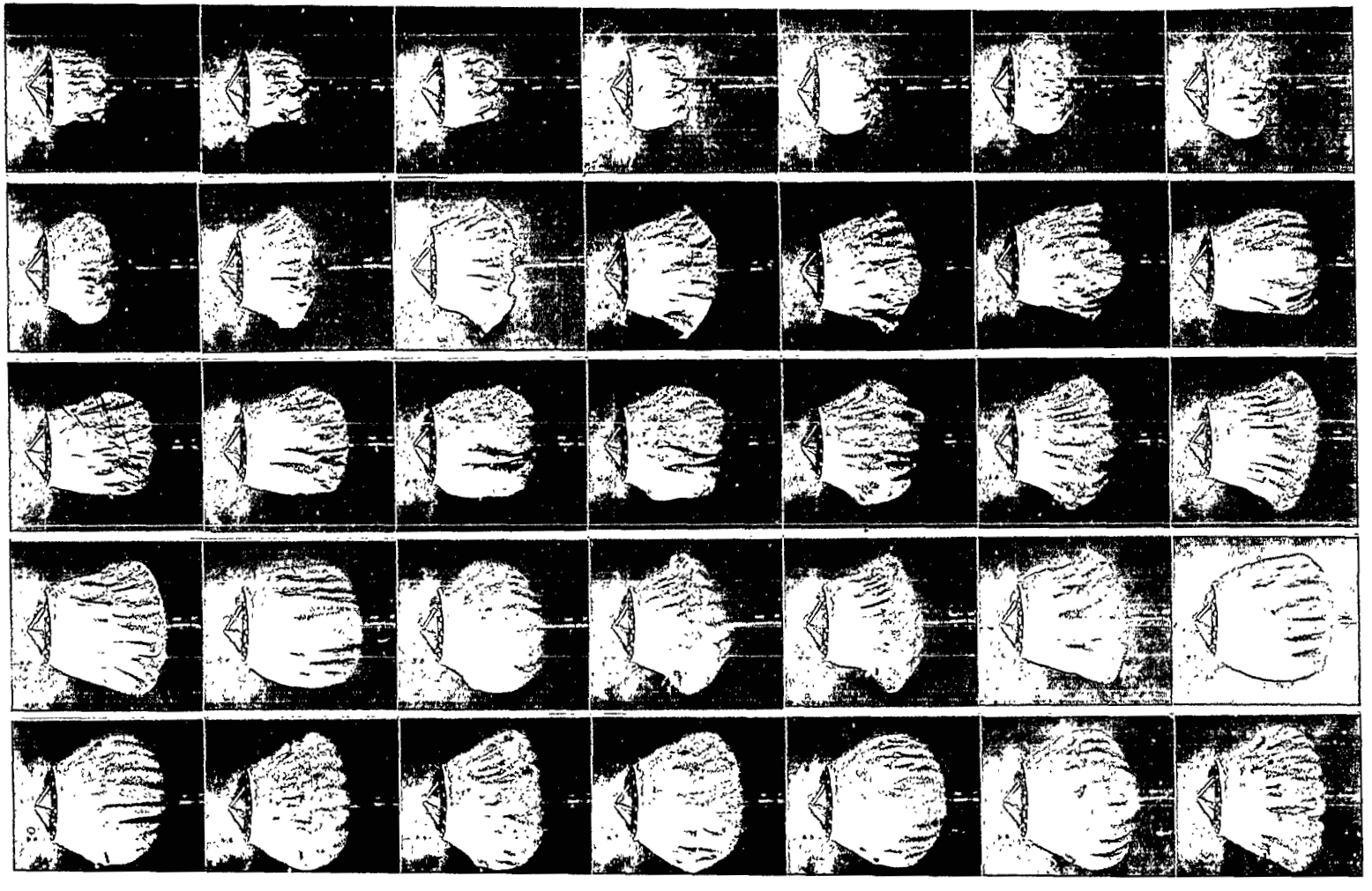

L-70-1558

Figure 22.- Attached inflatable decelerator model during ram inflation at Mach 3.0 and free-stream dynamic pressure of 1556 psf (74 kN/m^2). Time interval between frames is 0.001 sec.

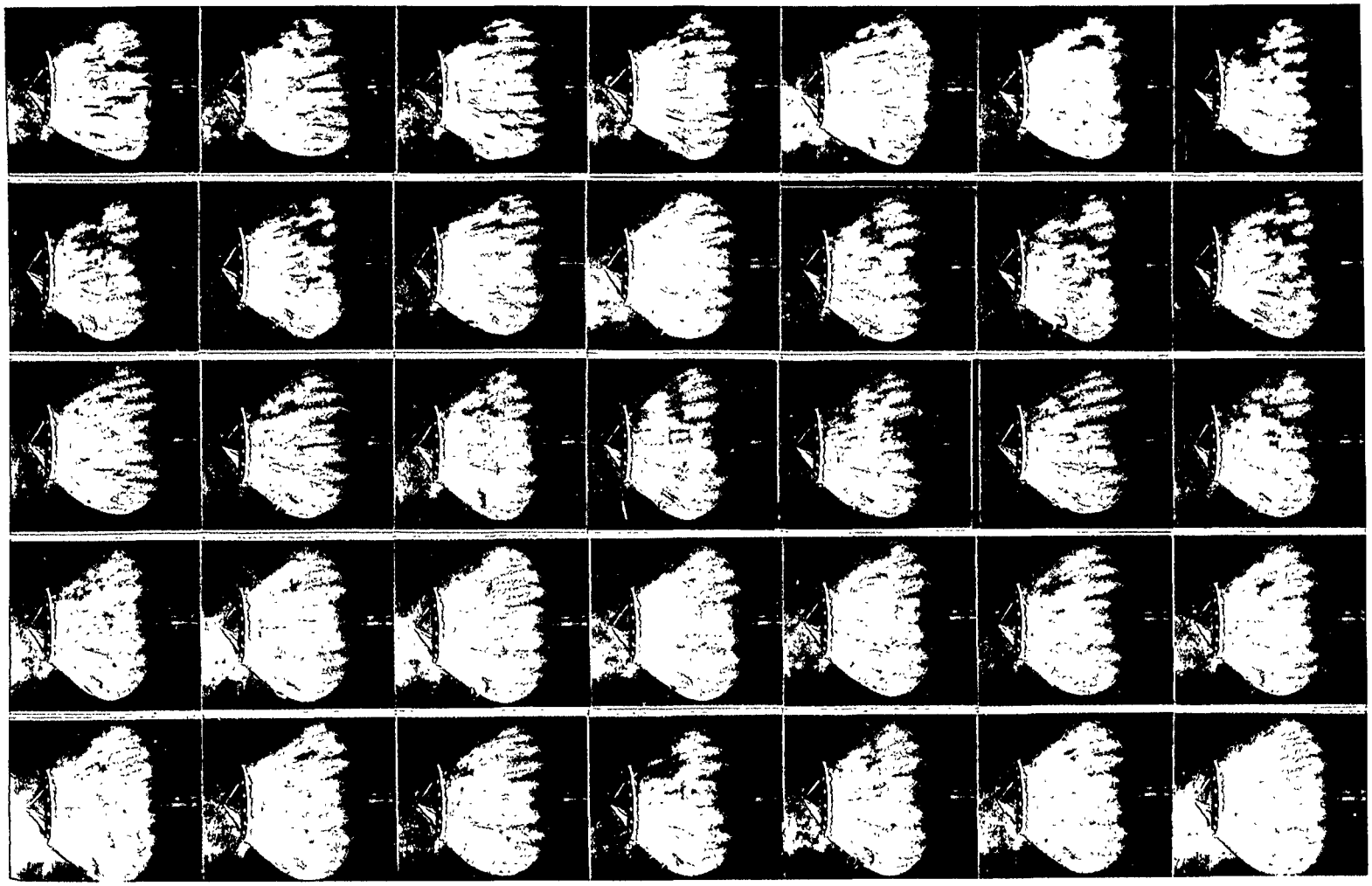

Figure 22.- Concluded. L-70-1559

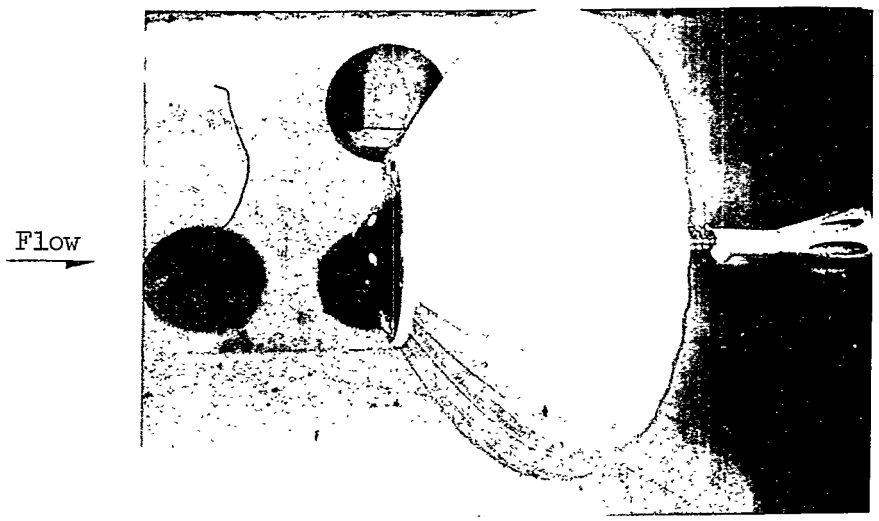

(a) Model with membrane-covered inlets. L-70-1560

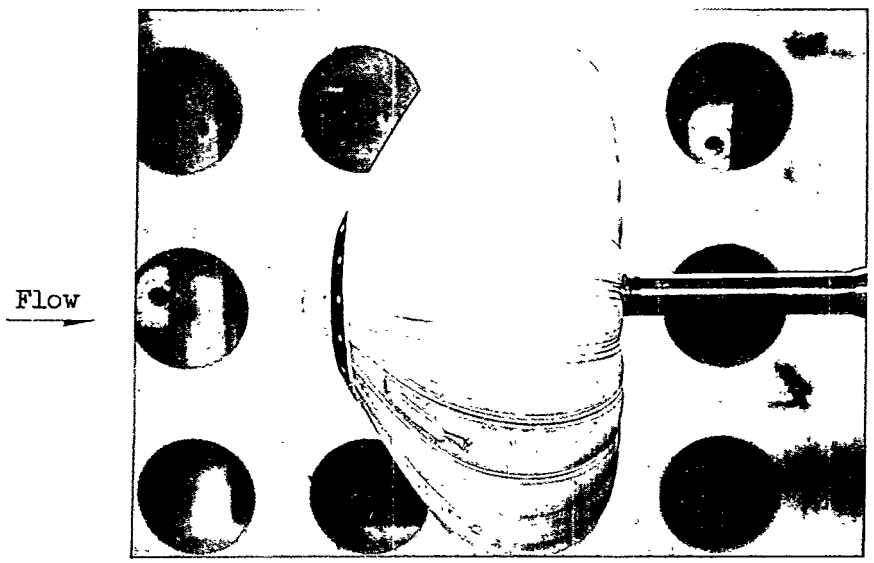

(b) Model with retractable nose-cone inlet. L-70-1561

Figure 23.- Ram-inflation models during wind-tunnel tests at a Mach number of 3.0 and a free-stream dynamic pressure of approximately 1500 psf (72 kN/m^2).

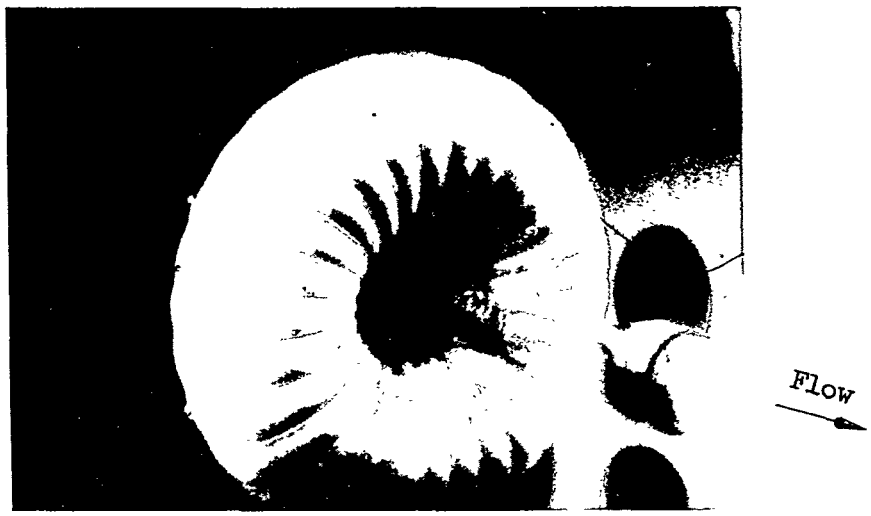

(c) Typical rear view. L-70-1562

Figure 23.- Concluded.

NATIONAL AERONAUTICS AND SPACE ADMINISTRATION
WASHINGTON, D. C. 20546

OFFICIAL BUSINESS

FIRST CLASS MAIL

POSTAGE AND FEES PAID
NATIONAL AERONAUTICS A
SPACE ADMINISTRATION

01U 001 26 51 3DS 70119 00903
AIR FORCE WEAPONS LABORATORY /WLOL/
KIRTLAND AFB, NEW MEXICO 87117

ATT E. LOU BOWMAN, CHIEF,TECH. LIBRARY

POSTMASTER: If Undeliverable (Section 158 Postal Manual) Do Not Retu

"The aeronautical and space activities of the United States shall be conducted so as to contribute . . . to the expansion of human knowledge of phenomena in the atmosphere and space. The Administration shall provide for the widest practicable and appropriate dissemination of information concerning its activities and the results thereof."

—NATIONAL AERONAUTICS AND SPACE ACT OF 1958

NASA SCIENTIFIC AND TECHNICAL PUBLICATIONS

TECHNICAL REPORTS: Scientific and technical information considered important, complete, and a lasting contribution to existing knowledge.

TECHNICAL NOTES: Information less broad in scope but nevertheless of importance as a contribution to existing knowledge.

TECHNICAL MEMORANDUMS: Information receiving limited distribution because of preliminary data, security classification, or other reasons.

CONTRACTOR REPORTS: Scientific and technical information generated under a NASA contract or grant and considered an important contribution to existing knowledge.

TECHNICAL TRANSLATIONS: Information published in a foreign language considered to merit NASA distribution in English.

SPECIAL PUBLICATIONS: Information derived from or of value to NASA activities. Publications include conference proceedings, monographs, data compilations, handbooks, sourcebooks, and special bibliographies.

TECHNOLOGY UTILIZATION PUBLICATIONS: Information on technology used by NASA that may be of particular interest in commercial and other non-aerospace applications. Publications include Tech Briefs, Technology Utilization Reports and Notes, and Technology Surveys.

Details on the availability of these publications may be obtained from:

SCIENTIFIC AND TECHNICAL INFORMATION DIVISION

NATIONAL AERONAUTICS AND SPACE ADMINISTRATION

Washington, D.C. 20546